Student thesis series INES nr 785

Multifaceted characteristics of arctic and boreal evapotranspiration in a warming world from multi-source remote sensing

Yaxian Yuan

2026
Department of
Earth and Environmental Sciences
Lund University
Sölvegatan 12
S-223 62 Lund
Sweden

Yaxian Yuan (2026).
Multifaceted characteristics of arctic and boreal evapotranspiration in a warming world from multi-source remote sensing
Master degree thesis, 30 credits in *Subject of degree*
Department of Earth and Environmental Sciences, Lund University

Level: Master of Science (MSc)

Course duration: *January* 2026 until *June* 2026

Multifaceted characteristics of arctic and boreal evapotranspiration in a warming world from multi-source remote sensing

---

Yaxian Yuan

Master thesis, 30 credits, in *GIS and Remote Sensing*

Supervisor name
Wenxin Zhang

Thesis evaluator:
Paul Miller

Course examiner:
Martin Berggren

Abstract

Total evapotranspiration (ET) trends remain highly consistent across FLUXCOM-X-BASE and GLEAM v4.2a, indicating a robust growing-season ET change in northern high latitudes. However, the mechanisms behind this change are less consistent than the total flux suggests. This thesis examines whether vegetation greening explains ET changes, whether ET components compensate for one another, and whether dry-wet ecosystem classifications represent process-level ET controls.

Growing-season ET north of 45°N from 2001 to 2020 was analyzed using FLUXCOM-X-BASE and GLEAM v4.2a, together with MODIS leaf area index (LAI), land surface temperature (LST), albedo, and the GLWD v2.0 dry-wet classification. The analysis focused on total ET trends, component partitioning, nonlinear temperature responses, and pixel-wise driver attribution.

Although total ET trends are broadly consistent between the two products, their inferred mechanisms differ substantially. Dry ecosystems show a near-compensatory substitution among ET components, whereas wet ecosystems show weak or nearly absent component changes. The direction of this substitution is broadly consistent with vegetation greening, but the relationship between pixel-level Ec/ET trends and LAI trends is very weak, with an R^2 of approximately 0.02. This suggests that greening alone cannot explain the magnitude of ET component changes, and that non-vegetation processes are also important.

ET responds nonlinearly to LST anomalies. A cold-end breakpoint near -9°C likely reflects constraints from snow cover and vegetation dormancy rather than water limitation. When stratified by latitude, an inverted-U warm-end response appears in the 45-55°N band for both dry and wet pixels, suggesting that the transition from energy limitation to water limitation follows a latitudinal gradient rather than the GLWD-defined dry-wet split.

Pixel-wise partial correlations further show that dry and wet ecosystems within the same latitude band have similar driver structures, with the largest dry-wet difference reaching only 0.08 absolute units for any single driver. Latitude separates ET controls more clearly: LST and soil moisture correlations strengthen toward higher latitudes, while LAI weakens slightly. Finally, driver attribution differs strongly between products. The LAI-dominant pixel share drops from 75% and 65% in dry and wet pixels under FLUXCOM-X-BASE to 34% and 29% under GLEAM v4.2a, whereas LST correlations remain relatively stable. This divergence likely reflects predictor circularity in FLUXCOM-X-BASE, whose machine-learning framework uses MODIS-derived variables that overlap with the driver set. Overall, total ET trends are robust across products, but mechanistic attribution is highly product-dependent. Future large-scale ET studies should therefore validate findings across multiple datasets and critically examine internal model assumptions before drawing causal conclusions.

Keywords: Evapotranspiration; Vegetation greening; Arctic; Remote sensing; Climate change; Global warming.

Acknowledgments

I would like to express great thanks to my supervisor, Wenxin Zhang, for his continuous guidance and feedback throughout this thesis, from choosing the topic, to designing the study, analysing the data, and writing it up. His careful advice on data choices, methodological rigour, and the structure of the analysis shaped what this thesis finally became.

I would also like to thank the Department of Physical Geography and Ecosystem Science at Lund University for the learning environment and computing resources provided over the past two years.

To my parents, thank you so much for quietly supporting me throughout my studies, thank you for all! And I'm also grateful to my friends, and classmates for standing by me during my master's studies and the completion of this thesis, it is their support that has carried me to where I am today.

Data Acknowledgments

This study contains modified Copernicus Climate Change Service information (2019). Neither the European Commission nor ECMWF is responsible for any use that may be made of the Copernicus information or data it contains.

This study also made use of several open data products, which are acknowledged here:

- MODIS products (MOD15A2H LAI, MOD11A2/MYD11A2 LST, MCD43A3 Albedo) were provided by the NASA EOSDIS Land Processes DAAC (LP DAAC) and accessed through the Google Earth Engine platform.
- FLUXCOM-X-BASE ET was released by the FLUXCOM team at the Max Planck Institute for Biogeochemistry.
- GLEAM v4.2a was developed and maintained by the Hydro-Climate Extremes Lab at Ghent University and archived on Zenodo.
- GLWD v2.0 was released by the McGill University team and obtained from figshare.
- ESA CCI Soil Moisture v09.1 (COMBINED product) was provided by the European Space Agency Climate Change Initiative and downloaded from the CEDA Archive.

Declaration of Generative AI

During the writing and analysis of this thesis, I used *Claude* from Anthropic (Claude Sonnet 4.5 and Claude Opus 4.6) as a supporting tool. Specifically, it was used for debugging Python code, translation between languages and language polishing. I also used *Grammarly* for grammar and spelling checking.

All AI-assisted content was reviewed and verified by me. The AI tools did not make any substantive judgements about the research results, nor were they used as a source of references.

List of Abbreviations

Data Products and Datasets

- ERA5-Land: ECMWF Reanalysis v5 — Land component
- ESA-CCI SM: European Space Agency Climate Change Initiative Soil Moisture
- FLUXCOM-X-BASE: FLUXCOM eXplainable BASE machine-learning upscaled flux product
- GLEAM: Global Land Evaporation Amsterdam Model (v4.2a)
- GLWD: Global Lakes and Wetlands Database (v2.0)
- MCD43A3: MODIS Combined Albedo product
- MOD11C3: MODIS Land Surface Temperature monthly product
- MOD15A2H: MODIS Leaf Area Index 8-day product
- MODIS: Moderate Resolution Imaging Spectroradiometer

Variables and Fluxes

- ET: Evapotranspiration
- Ec: Canopy transpiration
- Es: Soil evaporation
- Ei: Interception loss
- Ec/ET: Transpiration fraction of ET
- Es/ET: Soil-evaporation fraction of ET
- LAI: Leaf Area Index
- LST: Land Surface Temperature
- ΔLST: LST anomaly (relative to per-pixel monthly climatology)
- ΔET: ET anomaly (relative to per-pixel monthly climatology)
- SM: Soil Moisture
- VPD: Vapour Pressure Deficit
- NDVI: Normalized Difference Vegetation Index

Methods and Statistics

- MK: Mann–Kendall trend test
- OLS: Ordinary Least Squares regression
- AIC: Akaike Information Criterion
- ΔAIC: Difference in AIC between competing models
- R^2: Coefficient of determination
- IQR: Interquartile Range
- SE: Standard Error
- GEE: Google Earth Engine

Geography and Time

- MJJAS: May–June–July–August–September (growing season window)
- °N: Degrees north (latitude)
- yr: Year

1 Introduction

High-latitude ecosystems are undergoing rapid warming and vegetation greening, fundamentally changing land–atmosphere interactions. The Arctic warmed at approximately four times the global average rate between 1979 and 2021 under the effect of arctic amplification (Rantanen et al., 2022). With this warming trend, satellite remote sensing has recorded widespread vegetation greening over the past four decades, primarily manifested as shrub expansion, lengthening of the growing season, and increases in leaf area index (LAI) (Berner et al., 2020; Frost et al., 2025) . The temperature limitation on vegetation growth has weakened significantly — between 1982 and 2012, the global area of vegetation subject to cold-temperature limitation decreased by 16% (Keenan & Riley, 2018). Understanding the climatic consequences of this greening trend requires a closer consideration of how vegetation changes alter the exchange of energy and moisture between the land surface and the atmosphere.

Vegetation changes feedback to the climate system through two parallel pathways: biogeophysical processes that alter the surface energy balance, and biogeochemical processes that alter atmospheric greenhouse gas concentrations (Bonan, 2008). Vegetation changes affect the surface energy budget primarily by two mechanisms on the biogeophysical side. The first is albedo, which is a measure of how much sunlight a surface reflects. When plants spread over previously snow-covered ground, the land turns darker. Darker surfaces absorb more solar energy, so the area warms up (Chapin et al., 2005). The second is ET: vegetation transports water to the atmosphere via transpiration while consuming surface energy in the form of latent heat. These two pathways push temperature in opposite directions. Which one wins out in a given area and season determines whether vegetation growth makes a region warmer or cooler (Zhang et al., 2014). Among these feedback mechanisms, ET is the key flux linking vegetation, the water cycle, and the energy balance, and is therefore the central focus of this study.

Specifically, ET integrates three components: soil evaporation (Es), plant transpiration (Ec), and canopy interception evaporation (Ei) (Yang et al., 2023). It is both the largest water output pathway of terrestrial ecosystems, returning over 60% of terrestrial precipitation to the atmosphere (Jung et al., 2010), and a key regulator of surface energy partitioning, with the associated latent heat flux consuming more than 50% of the net radiation at the land surface (Yang et al., 2023). In recent decades, global ET has been accelerating: diagnostic datasets show that the growth rate of ET has increased from 0.66 ± 0.38 mm yr^{-2} during 1982–2011 to 1.19 ± 0.31 mm yr^{-2} during 2001–2020, with the largest increases concentrated in the boreal high-latitude regions where vegetation greening has been most pronounced (Yang et al., 2023).

However, the increase in total ET does not reveal whether water leaves the surface through plant transpiration or soil evaporation. At the global scale, plant transpiration accounts for approximately $64 \pm 13\%$ of total ET (Good et al., 2015), but this proportion varies greatly across ecosystems and is strongly controlled by vegetation structure — LAI can explain approximately 43% of the inter-ecosystem variation in T/ET (L. Wang et al., 2014). Notably, this control is not linear: in high-LAI areas, the simultaneous increase in canopy interception

loss partially offsets transpiration gains, leading to a saturation effect in T/ET (L. Wang et al., 2014; Yang et al., 2023). This implies that, as high-latitude vegetation continues to green, the component structure of ET — i.e., the ratios of Ec/ET and Es/ET — may be undergoing a systematic reorganization, and the direction of this reorganization will determine whether vegetation greening enhances evaporative cooling or promotes sensible heating. At present, such component-level analysis of ET changes is virtually absent for high-latitude regions.

Although both models and observations confirm that vegetation across the northern latitudes is greening, they yield markedly different conclusions regarding the direction and climatic effects of ET changes. Regional Earth system models generally predict that vegetation greening enhances ET by increasing LAI and reducing albedo, and that the resulting evaporative cooling in summer can partially offset (by up to ~0.81 °C) the warming intensified by albedo reduction in winter and spring (by up to ~1.35 °C) (Bonfils et al., 2012; Zhang et al., 2014). However, Lafleur & Humphreys (2018), using eddy covariance measurements over six growing seasons at three tundra sites with varying shrub cover in the Canadian Low Arctic, found that the site with the highest shrub cover showed no significant difference in cumulative latent heat flux compared to the low-cover sites, whereas sensible heat flux was significantly higher — the excess absorbed energy was not used for evaporative cooling as models predicted, but instead directly heated the atmosphere. Mekonnen's review study pointed out that the effect of shrub expansion on ET is highly dependent on moisture availability, and that under dry conditions, shrubs may suppress transpiration by closing stomata rather than enhancing it (Mekonnen et al., 2021). This points to a deeper issue: the northern high-latitude domain is dominated by dry uplands, while wetlands cover only about 14% of the land area (Olefeldt et al., 2021), and these two ecosystem types differ fundamentally in moisture supply and energy partitioning, yet existing models and large-scale analyses rarely distinguish between them.

This difference is primarily reflected in the distinct ET response logic of the two system types to warming. In wet ecosystems, where moisture is abundant, ET is mainly driven by available energy. Helbig(2020; 2020) found that peatlands can have ET up to 30% higher than adjacent forests under high VPD conditions, and their unique surface properties cause peatland landscapes to be 1.7–2.5 °C cooler than forests during the growing season, largely consistent with the evaporative cooling pathway. However, in dry ecosystems, moisture availability is the fundamental constraint on ET. When soil moisture falls below a critical threshold, plants close their stomata and ET declines rather than increases (Seneviratne et al., 2010). Evidence at the global scale indicates that this transition from energy limitation to water limitation is accelerating (Denissen et al., 2022; Jiao et al., 2021). In high-latitude dry systems, permafrost meltwater can contribute up to 17.6% of growing-season ET during dry years, partially buffering the moisture constraint (Park et al., 2021), but as permafrost degradation accelerates, this buffering effect is also weakening. Because Earth system models typically do not treat wetlands as an independent functional type (Helbig, Waddington, Alekseychik, Amiro, Schulze, et al., 2020), and most large-scale analyses use spatial resolutions (≥0.5°) insufficient to distinguish dry and wet pixels, the above divergent mechanisms are masked.

Although the aforementioned studies have revealed trends in total ET and its response mechanisms, research on changes in the component structure of ET at high latitudes remains limited. In terms of component structure, how the individual ET components (Ec, Ei, Es) differentially change along the dry–wet ecosystem gradient in response to vegetation greening currently has almost no observational evidence at high latitudes, while Li et al. (2026) noted that the sensitivity of ET to LAI is declining globally. Meanwhile, Fu et al. (2024) have demonstrated that the critical soil moisture threshold (θ_{crit}) exhibits spatial heterogeneity, but whether a nonlinear threshold in the temperature–ET relationship exists along high-latitude dry–wet gradients has not yet been tested. More fundamentally, whether ecosystems under different moisture conditions are controlled by systematically different driving factors still lacks direct evidence at high latitudes; and the spatial compensation effect revealed by Jung et al. (2017) suggests that large-scale analyses that do not distinguish ecosystem types will obscure the true controlling mechanisms. These unresolved questions motivate the present study, whose specific aims and hypotheses are outlined in the following section.

2 Research Aim and Hypotheses

2.1 Aim

This study examines how ET has changed across the northern Hemisphere above 45°N between 2001 and 2020, using data from multiple remote sensing sources. Most existing studies treat total ET as a single number. This study goes further by separating ET into its components and asking how vegetation greening has reshuffled the balance between them. Apart from that, this study also examines how temperature and ET related to each other, and whether this relationship shifts across latitudes. Finally, it asks which environmental factors most strongly drive ET changes, and whether dry and wet ecosystems follow different rules.

2.2 Hypotheses

H1: In dry ecosystems, soil evaporation accounts for a large share of total ET since the canopy is sparse. When vegetation expands and leaf area increases, the canopy starts intercepting incoming radiation before it reaches the soil surface. Soil evaporation therefore drops, and transpiration takes over a larger fraction of total ET, thus the Ec/ET ratio rises (Yang et al., 2023). In wet ecosystems, water supply is not a limiting factor there, so transpiration is already high before any greening occurs. Adding more leaf area does not push transpiration much further, partly because denser canopies also increase interception losses. The transpiration fraction therefore stays relatively flat even as vegetation grows (H. Li et al., 2026; Yang et al., 2023).

Testable predictions: (i) Dry pixels show a significant positive Ec/ET trend and a corresponding negative Es/ET trend over 2001–2020; wet pixels show near-zero trends in both ratios. (ii) The slope linking LAI trend to Ec/ET trend is steeper in dry than in wet ecosystems. (iii) The sensitivity of ET to LAI (∂ET/∂LAI) decreases with increasing LAI, consistent with a saturation effect, and this decay is evident in both ecosystem types.

H2: The temperature–ET relationship is nonlinear in dry ecosystems. In wet ecosystems, energy supply is the main bottleneck for ET. More warmth means more energy available to drive evaporation and transpiration, so ET rises steadily with temperature. In dry ecosystems, temperature still drives ET upward at the cooler end. However, after a certain point, rising temperatures push water demand beyond what the soil can supply. At that stage, ET stops increasing and may decline (Denissen et al., 2022; Seneviratne et al., 2010).

Testable predictions: (i) A piecewise or quadratic model fits the temperature–ET relationship better than a linear model in dry ecosystems, whereas a linear model adequately describes wet ecosystems. (ii) At the warm end of the temperature range, ET flattens or declines in dry pixels but not in wet pixels. (iii) When data are split by latitude band, the thermal threshold appears first in the 45–55°N zone, where dry ecosystems reach the highest absolute temperatures.

H3: Dominant environmental drivers of ET differ between ecosystem types, reflecting the underlying contrast between energy-limited and water-limited regimes (Denissen et al., 2022; Seneviratne et al., 2010). In wet ecosystems, where soil moisture is generally above the threshold for stomatal regulation, ET variability is expected to be controlled primarily by energy supply and the size of the transpiring surface, with land surface temperature (LST, as a proxy for available energy) and leaf area index (LAI) acting as the leading partial correlates. In dry ecosystems, water availability is expected to exert a stronger constraint, with soil moisture (SM) and precipitation (Precip) showing partial correlations of larger absolute magnitude than in wet ecosystems. Surface albedo is included as a fifth candidate driver to represent the radiation-balance signal, although its independent role is expected to be modest once LST is controlled for.

Testable predictions: (i) The median partial correlation between ET anomalies and water-related drivers (SM and Precip) is larger in absolute magnitude in dry ecosystems than in wet ecosystems. (ii) The median partial correlation between ET anomalies and LST is larger in wet ecosystems than in dry ecosystems. (iii) The dominant-driver distribution differs categorically between the two ecosystem types: water-related drivers (SM, Precip) account for a larger share of dry pixels, while energy-related drivers (LST) account for a larger share of wet pixels. (iv) These contrasts are reproducible when the analysis is repeated with GLEAM v4.2a in place of FLUXCOM-X-BASE as the ET product.

3 Theoretical Background

3.1 ET Partitioning: Mechanisms and Controls

ET is the process by which water transitions from liquid to gas and leaves the land surface. This phase change consumes latent heat energy, placing ET at the crossroads of the water cycle and the energy cycle. Water can leave the land surface through three pathways: soil evaporation (Es), plant transpiration (Ec), and canopy interception evaporation (Ei). Soil evaporation does not require the involvement of vegetation. It is the main ET pathway in bare or sparsely vegetated areas. During rainfall, a portion of precipitation is intercepted by leaves and branches, and evaporates straight back into the atmosphere before it ever reaches the soil. Among the three components, plant transpiration is the most strongly controlled by plant physiology: roots extract water from the soil, which is then released as water vapour through stomata. These same stomata also let CO_2 in for photosynthesis, which means transpiration and carbon uptake are tied together. At the global scale, transpiration is the largest component, accounting for approximately 59–64% of total ET (Good et al., 2015; Yang et al., 2023).

Leaf area index (LAI), defined as the total one-sided area of leaf tissue per unit ground surface area, is the key variable that controls how ET is partitioned among these three components. However, the influence of LAI on partitioning is not in the same direction. It affects each one differently, and the combined result is nonlinear:

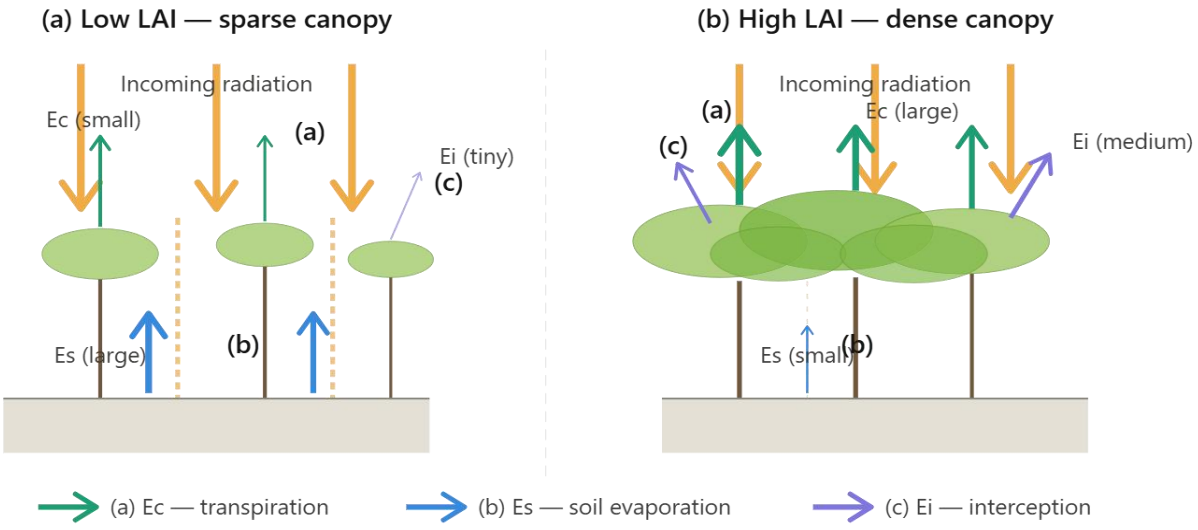

Figure 2.1. Schematic illustration of how leaf area index (LAI) regulates the three components of evapotranspiration. (a) Low LAI (sparse canopy): transpiration (Ec) is small, soil evaporation (Es) is large, and interception (Ei) is negligible. (b) High LAI (dense canopy): Ec increases as transpiring leaf area expands, Es decreases as canopy shading reduces radiation reaching the soil surface, and Ei increases with greater canopy water storage capacity.

Pathway (a): Increasing LAI enhances Ec. More leaf area gives the canopy a larger surface through which water can escape. Beyond that, a denser canopy captures more incoming radiation, making stomata open wider and staying open longer, which drives transpiration up.

Pathway (b): Increasing LAI reduces the proportion of soil evaporation. Radiation is the energy source driving soil evaporation. As the canopy fills in, less radiation gets through to the soil surface. Soil evaporation therefore drops, and its share of total ET shrinks.

Pathway (c): Increasing LAI enhances Ei. A denser canopy has a larger surface area to catch rainfall and hold water. Under the same precipitation, canopy with higher LAI therefore loses more water through direct evaporation from wet leaf surfaces before any of it reaches the soil.

When LAI is low, Pathway (a) dominates: Ec rises faster than Ei, so the Ec/ET ratio climbs. When LAI is already high, this changes. Lower canopy layers receive progressively less light, and each additional leaf contributes less to transpiration — Ec growth slows down. Ei, however, keeps scaling with canopy surface area. At some point, the two offset each other, and Ec/ET levels off or even falls. Yang et al. (2023) call this the "saturation effect" in T/ET. Wang et al. (L. Wang et al., 2014) found the same pattern across different ecosystem types. Li et al. (2026) using observation-constrained CMIP6 projections, further show that the global sensitivity of ET to LAI ($\partial ET/\partial LAI$) is weakening, especially in regions with high LAI and high temperatures.

This mechanism is the direct basis for H1 in this study. In dry ecosystems, where the canopy is sparse and LAI is low, a large fraction of incoming radiation reaches the exposed soil surface; consequently, Es constitutes a large share of total ET and Ec/ET is low. When greening occurs, pathways (a) and (b) operate simultaneously — transpiration increases while soil evaporation decreases — and we expect to observe rising Ec/ET and declining Es/ET, a process termed component substitution. In wet ecosystems, by contrast, Ec/ET is already near its saturation level; the marginal contribution of additional LAI to transpiration is offset by the concurrent increase in interception evaporation, and Ec/ET therefore remains largely unchanged. Understanding this differential response of ET components to LAI changes is thus a prerequisite for distinguishing the climate feedback effects of dry versus wet ecosystems.

To quantify such component-level changes across the high latitudes, globally gridded products capable of decomposing total ET into its constituent fluxes are required. The Global Land Evaporation Amsterdam Model (GLEAM) is one of the few products that independently provides physically based estimates of transpiration (Et), bare soil evaporation (Eb), and interception loss (Ei) at global scale, and is therefore employed in this study for testing H1 (Miralles et al., 2025b). GLEAM estimates ET and its components through four sequential modules. First, the interception module uses satellite-observed LAI and fraction of absorbed photosynthetically active radiation (fPAR) to constrain a van Dijk–Bruijnzeel interception model, computing the amount of rainfall intercepted by the canopy and subsequently evaporated — this corresponds to pathway (c) described above. Second, the potential evaporation module calculates the upper limit of atmospheric evaporative demand using the Penman equation, integrating net radiation, air temperature, wind speed, VPD, and vegetation height. In the soil water module, root-zone water content is tracked through a multi-layer running water balance model and constrained by assimilating ESA CCI satellite microwave soil moisture observations. Finally, the evaporative stress module uses a deep neural network trained on global eddy-covariance and sap-flow data. The network outputs a stress factor S,

which runs from 0 to 1 and scales potential evaporation down to actual evaporation. By computing S separately for bare soil, tall vegetation, and short vegetation, GLEAM produces separate estimates of transpiration and soil evaporation rather than a single combined flux. For bare soil evaporation specifically, GLEAM applies the Beer-Lambert law to work out how much incoming radiation gets through the canopy and actually hits the soil surface. A higher LAI means a denser canopy, less radiation reaching the soil, and therefore less energy available to drive soil evaporation. This is exactly the shading mechanism described in Pathway (b), built directly into the model structure.

3.2 Non-linear ET Responses to Warming

The Penman–Monteith equation (Monteith, 1965) describes ET as driven by two forces: net radiation, which supplies the energy needed to turn liquid water into vapour, and atmospheric demand, measured by vapour pressure deficit (VPD). As temperature rises, saturation vapour pressure increases exponentially following the Clausius–Clapeyron relation, and VPD climbs sharply with it. Both driving forces therefore strengthen with warming, and under purely physical reasoning, ET should rise steadily with temperature. In practice, water availability changes this picture.

Whether a system is energy-limited or water-limited determines how ET actually responds to warming. This distinction goes back to the work of Budyko (1974) and was developed more fully by Seneviratne et al. (2010) in their review of soil moisture–climate feedbacks. When soil moisture is sufficient, water supply is not the bottleneck. ET is bounded by available energy, and rising temperatures push it upward in a roughly linear way. In dry conditions, the logic breaks down. Warming still increases VPD and radiation, but the soil cannot supply enough water to keep up. Past a certain temperature threshold, ET stops rising and begins to fall.

The boundary between these two states corresponds to the framework described by Budyko: in very dry regions, actual evaporation approaches precipitation (water limitation), whereas in very wet regions, actual evaporation approaches potential evapotranspiration (energy limitation).

The key mechanism behind this reversal is stomatal closure. Stomata control both water vapour loss and CO_2 uptake, and they respond directly to soil moisture. When root-zone moisture drops below a critical level (θ_{crit}), roots release abscisic acid (ABA), which travels to the leaves and triggers stomata to close — a protective response that limits water loss before the plant reaches lethal dehydration. Seneviratne et al. (2010) identified θ_{crit} as the point where a system crosses from energy limitation into water limitation. Denissen et al. (2022) using global observational data, showed that this threshold is not a fixed number but varies widely across space, and that Earth system models suggest the transition from energy-limited to water-limited conditions is speeding up globally.

This transition matters especially in the high latitudes, where it is often overlooked. Dry uplands account for approximately 80% of the land surface north of 45°N, while wetlands constitute only about 14% (Olefeldt et al., 2021). Water limitation is therefore the norm for

most of this region, not the exception. However, the rising ET trends reported in global reviews (Yang et al., 2023) largely reflect humid areas. For high-latitude dry systems, permafrost meltwater can cover 12–18% of growing-season ET during dry years, acting as a buffer that delays the ET decline (Park et al., 2021). As permafrost continues to degrade, however, this buffer will not hold indefinitely.

This creates a spatial gradient worth testing. In the mid-latitudes of the study domain, where permafrost is thin or already degraded, water limitation effects should emerge sooner. At higher latitudes where deep permafrost remains intact, the transition may be delayed. If this reasoning holds, the temperature threshold at which ET stops increasing should shift predictably along a latitudinal gradient. H2 of this study tests whether that gradient exists.

3.3 Arctic Biogeophysical Feedbacks

ET changes feed back into climate warming, instead of just being a response. As the most prominent structural change in Arctic vegetation, shrub expansion changes two key terms of the surface energy balance. On one hand, taller shrubs extend above the snowpack and shade the surface. This reduces albedo, so more shortwave radiation gets absorbed rather than reflected, and near-surface temperatures rise further. Chapin et al. (2005) demonstrated that earlier snowmelt and the expansion of low-albedo vegetation together advanced the onset of sensible heating in the lower atmosphere over Arctic Alaska, constituting a positive feedback to warming. On the other hand, increased leaf area generally enhances transpiration during the growing season, which channels a greater fraction of available energy into latent heat flux and thus exerting an evaporative cooling effect on the surface (Zhang et al., 2014). The net climatic outcome of shrub expansion therefore depends on the relative magnitude of these two opposing mechanisms, which operate on different seasonal timescales: the albedo feedback dominates in winter and spring when snow-vegetation contrast is greatest, whereas the ET-mediated cooling is confined to the summer growing season.

Regional Earth system modelling has provided quantitative estimates of these competing effects. Zhang et al. (2014) uses the coupled RCA-GUESS model forced under a high-emission scenario and found that, the albedo feedback amplified spring near-surface warming by up to ~1.35 °C, while the evapotranspiration feedback produced a summer cooling of up to ~0.81 °C. The summer cooling arises because denser vegetation cover increases both total leaf area and surface roughness, which increases both transpiration and the energy exchange with atmosphere. The lower albedo leads to the warming in winter and spring, but partially offset by summer evaporative cooling. This seasonal compensation also extends the growing season, promotes vegetation productivity and reinforces the feedback cycle.

However, field observations have challenged this model-based mechanism. Lafleur and Humphreys (2018) based on eddy covariance measurements at three closely located tundra sites with varying shrub cover in the Canadian Low Arctic, found that evapotranspiration did not increase with shrub abundance at the lower-albedo sites; the additional available energy was instead partitioned into sensible heat flux, directly warming the atmospheric boundary layer. They attributed this to two coexisting mechanisms — canopy shading that suppresses

soil evaporation, and reduced stomatal conductance under high vapour pressure deficit. The discrepancy between modelled ET enhancement and observed sensible heat dominance shows a critical knowledge gap.

The answer to such a difference may lie in the differentiation between dry and wet ecosystems. Mekonnen et al. (2021) showed that the effect of shrub expansion on transpiration depends on slope hydrological conditions. At ridges, water stress limits both shrub growth and transpiration. On mid-slopes, higher soil moisture supports greater productivity and allows transpiration to increase. The same pattern holds when comparing dry and wet ecosystems more broadly. In drier systems, the energy freed up by lower albedo tends to go into sensible heat rather than evaporation, so the expected boost in transpiration does not materialise. In wetter systems, that extra energy can actually drive transpiration up. In other words, water availability determines the direction of biogeophysical feedback, and this is precisely what motivates the dry-wet comparison at the centre of this study.

4 Methods

4.1 Study Area

This study covers the northern high-latitude land area north of 45°N at a spatial resolution of 0.05°. The time window runs from 2001 to 2020 — 2001 marks when MODIS-era satellite products (LAI, LST, and albedo) became consistently available, and 2020 gives a 20-year record long enough for trend detection. All analyses focus on the boreal growing season, defined here as May through September (MJJAS). This window captures the period of active vegetation growth, snowmelt, and most of the annual ET at high latitudes (Bhatt et al., 2017). A common 0.05° grid was used as the common spatial framework across all datasets.

4.2 Data Sources

4.2.1 MODIS Data

The remote sensing variables LAI, LST, and albedo were all derived from MODIS satellite products, accessed via the Google Earth Engine (GEE) data catalogue:

- **LAI** was taken from the MOD15A2H Version 6.1 product (Myneni et al., 2021), an 8-day composite at 500 m resolution from the Terra platform.
- **Daytime LST** came from MOD11A2 (Terra) and MYD11A2 (Aqua) Version 6.1 (Wan et al., 2021), both 8-day composites at 1 km resolution. Before spatial aggregation, the two sensors were merged together. At high latitudes, persistent cloud cover means a single satellite typically captures only 2–3 usable scenes per month. Combining both sensors fills in the gaps and improves temporal coverage.
- **Shortwave white-sky albedo** was obtained from the MCD43A3 Version 6.1 product (Schaaf & Wang, 2021), a daily Terra+Aqua combined dataset at 500 m resolution.

All three products were quality-filtered, aggregated to monthly means, and resampled to 0.05° in GEE. For LAI, the *FparLai_QC* band was used to retain only pixels processed by the main algorithm; pixels with raw values exceeding 100 (corresponding to LAI > 10 m^2 m^{-2}) were removed. However, the filter was later found to be overly restrictive, causing a substantial number of pixels to be excluded. The data are currently being reprocessed, though trend directions are not expected to be affected. For LST, pixels with *QC_Day* lowest two bits equal to 00 (good) or 01 (reasonable) were retained, and raw values were converted to degrees Celsius (DN × 0.02 − 273.15). For albedo, the *BRDF_Albedo_Band_Mandatory_Quality_shortwave* band was used to retain only full BRDF inversion (0) and magnitude inversion (1) retrievals, with values scaled by 0.001. All variables were exported as multi-band GeoTIFFs covering 2001–2020.

4.2.2 Evapotranspiration: FLUXCOM-X-BASE

Total ET estimates were taken from the FLUXCOM-X-BASE product (Nelson et al., 2024), the most recent generation of the FLUXCOM family. FLUXCOM-X-BASE upscales eddy-

covariance measurements from the FLUXNET network to the global grid using XGBoost, with predictor variables comprising core meteorological data (2-m air temperature, incoming shortwave radiation, and vapor pressure deficit), plant functional type classification, MODIS-derived vegetation indices, and MODIS land surface temperature (Nelson et al., 2024). The product provides ET at 0.05° spatial resolution with hourly native temporal resolution; monthly aggregates were used in this study, covering 2001–2020. FLUXCOM-X served as the primary ET data source for trend analysis in this study, and was also used for cross-comparison with GLEAM (see Section 4.2.3). The inclusion of MODIS LST and MODIS-derived vegetation indices among the training predictors has implications for the partial correlation analysis in Section 4.3.3, which are addressed in the methodological considerations of the Discussion.

4.2.3 ET Partitioning: GLEAM v4.2a

To decompose total ET into its component fluxes, data from the Global Land Evaporation Amsterdam Model version 4.2a (Martens et al., 2017; Miralles et al., 2025a) were used. GLEAM v4.2a is a process-based, satellite-data-driven model that provides separate estimates of transpiration (E_t), bare soil evaporation (E_b), interception loss (E_i), and total evaporation (E) at 0.1° spatial resolution and daily temporal resolution, with monthly aggregates also available. The 'a' archive, which combines reanalysis and satellite forcing data covering 1980–2023, was used. Monthly files for E, E_t, E_b, and E_i were downloaded for 2001–2020 and clipped to the northern high-latitude domain (> 45°N); units are mm month^{-1}. GLEAM served two roles in this study: first, its component fluxes (E_t and E_b) were used to compute the transpiration fraction (E_c/ET) and soil evaporation fraction (E_s/ET) for testing H1; second, its total ET provided an independent check on the FLUXCOM-X trend results, allowing assessment of whether the detected signals are consistent across products with fundamentally different estimation approaches.

4.2.4 Ecosystem Classification: GLWD v2.0

A binary dry–wet ecosystem mask was constructed from the Global Lakes and Wetlands Database version 2.0 (Lehner et al., 2025), which provides wetland area percentage at roughly 500 m resolution globally. The original raster was clipped to the northern high-latitude domain (> 45°N) and aggregated to the 0.05° target grid using block-average resampling. Each grid cell received a continuous wetland fraction between 0 and 1. Cells with a wetland fraction at or above 0.50 were labelled wet; the rest were labelled dry. This threshold produced roughly 2.42 million dry pixels and 0.40 million wet pixels across the study domain. Both the binary mask and the continuous fraction were saved, so that alternative thresholds can be tested later without re-running the aggregation.

4.2.5 Soil Moisture and Precipitation: ERA5-Land

Soil moisture and precipitation drivers were drawn from the ERA5-Land monthly reanalysis (Copernicus Climate Change Service, 2019; Muñoz-Sabater et al., 2021) on its native 0.1° grid. Volumetric soil water in the top 0–7 cm layer (variable *swvl1*, m³ m^{-3}) was used as the SM driver, and total precipitation (variable *tp*) was used as the Precip driver, converted from m

day⁻¹ to mm day⁻¹. Both fields were extracted for the MJJAS months of 2001–2020 (100 monthly fields per variable).
ERA5-Land SM is not part of the FLUXCOM-X-BASE predictor set (Nelson et al., 2024) or the primary forcing of GLEAM v4.2a, and is therefore independent of both products. ERA5-Land precipitation is not a direct predictor in either product, but shares the ERA5 reanalysis backbone with FLUXCOM-X-BASE's meteorological forcing, so a partial overlap at the forcing level remains; the implications are addressed in §6.4.1..

4.3 Statistical Methods

4.3.1 Pixel-wise Trend Analysis and Greening–ET Coupling (H1)

This study applied pixel-wise trend analysis over the MJJAS growing season. For each pixel, MJJAS monthly values were averaged within each year, producing a 20-year annual time series.

Trends were detected using the Mann-Kendall test (Kendall, 1975; Mann, 1945), which does not assume a normal distribution and handles outliers well in short hydroclimatic records. The trend magnitude was estimated by the Theil-Sen slope estimator (Sen, 1968), defined as the median of all pairwise slopes across the 20-year record. This approach reduces the pull of any single anomalous year. Pixels with a significant trend were identified at $\alpha = 0.05$. Pixels with fewer than 15 valid annual values or zero variance were excluded.

Trend analysis was run separately for dry and wet pixels using the GLWD-derived mask. To test whether the two ecosystems produced statistically different slope distributions, a two-sided Mann-Whitney U test was applied.

To test whether pixels with stronger greening also show larger ET changes, the Sen's slope of MJJAS LAI was regressed against the Sen's slope of MJJAS ET at the pixel level using ordinary least-squares regression, again run separately for dry and wet pixels. Both Pearson and Spearman correlation coefficients were calculated. A parallel regression was then run replacing ET slope with the trend in transpiration fraction (Ec/ET) from GLEAM, to test whether greening shifts the ET composition toward transpiration.

A mass-balance closure diagnostic served to verify whether the opposite trends in Ec/ET and Es/ET across dry ecosystems reflect an actual ecological process, rather than a mere computational artifact of GLEAM. By design, GLEAM splits total ET into transpiration (Et), bare-soil evaporation (Eb), and interception loss (Ei). The fractions of these three components always sum to 1. If the dataset strictly enforced this mathematical closure at the pixel level, any increase in the Ec/ET fraction would algebraically force a decrease in the remaining components.

To test this possibility, the present analysis applied the same Mann–Kendall and Theil–Sen trend procedures to the Ei/ET fraction. The spatial domain, growing-season timeframe, and validity thresholds remained identical to the earlier steps. Summing the slopes of all three fractions yielded the pixel-level closure residual (r). The median, mean, and 95th percentile of

the absolute residual values effectively captured the distribution of this metric.The underlying logic is straightforward. A minimal residual (less than 5% of the Ec/ET trend) means strict algebraic closure, which implies the observed dynamic between components acts partly as an arithmetic consequence. The residual over 30% confirms the independent estimation of these component trends by the model.The observation changes in the proportional balance among the ET fractions thus point to an actual ecological process.

Since FLUXCOM-X-BASE upscales eddy-covariance measurements to global coverage via machine-learning regression, an independent sensitivity check was performed using GLEAM v4.2a, which is produced by a different methodological framework. The same trend detection procedure was applied, and the resulting slope distributions and significance proportions were compared with those from FLUXCOM-X-BASE to assess the robustness of H1 findings across independent ET products.

4.3.2 Anomaly-based Binned Regression of the Temperature–ET Response (H2)

The temperature–ET response was characterized by fitting competing models and applying AIC-based selection to determine whether the response is linear, nonlinear, or contains a breakpoint.Since this study pools observations from millions of pixels over 100 time steps (20 years × 5 months), directly using absolute LST and ET values would be problematic: the absolute LST–ET relationship is dominated by spatial gradients in background climate, as pixels at lower latitudes are inherently warmer and support higher ET than those at higher latitudes. This spatial covariance would produce a strong positive LST–ET relationship in the binned response curve that primarily reflects the geographic distribution of pixels within each temperature bin, rather than the sensitivity of ET to temperature variation.

To get around this, an anomaly framework was used. For each pixel, a 20-year MJJAS climatology mean was calculated for both ET and LST (2001–2020). Each observation was then expressed as a departure from that pixel-specific mean ($\Delta LST = LST - \overline{LST}$; $\Delta ET = ET - \overline{ET}$). Pixels with fewer than 10 valid monthly observations were dropped. The absolute LST–ET relationship was kept separately as a reference.

The ΔLST range was divided into equal-width bins of 2° C. Within each bin, the mean and standard error of ΔET were calculated separately for dry and wet ecosystems. Bins with fewer than 50 observations were dropped. Given the large data volume, a single-pass algorithm was used that tracked running sums, sums of squares, and counts per bin without loading everything into memory at once.

Three regression models of increasing complexity were then fitted to each binned response curve, with bin-center ΔLST as the predictor and bin-mean ΔET as the response:

(1) A linear model ($\Delta ET = a + b \cdot \Delta LST$; 2 parameters): It assumes ET sensitivity to temperature stays constant across the full anomaly range.

(2) A quadratic model ($\Delta ET = a + b \cdot \Delta LST + c \cdot \Delta LST^2$; 3 parameters): It allows for a curved response. The vertex temperature $T\_v = -b/(2c)$ marks the anomaly at which ET peaks or turns around. A negative coefficient c means ET rises with warming up to T_v, then falls — a pattern consistent with moisture stress at high temperatures.

(3) A piecewise linear model ($\Delta ET = a + b_1 \cdot \min(\Delta LST - bp, 0) + b_2 \cdot \max(\Delta LST - bp, 0)$; 4 parameters). Rather than a smooth curve, this model allows temperature sensitivity to shift at a single breakpoint (bp). The best breakpoint was found by minimizing the residual sum of squares across all candidate values within the 15th–85th percentile range of bin centers. Restricting the search to this range avoids unstable fits at the ends where data are sparse. The model was fitted using ordinary least squares. This setup can capture patterns like a steep rise at cold temperatures followed by a flat response at warm ones.

The three models were compared using the Akaike Information Criterion (AIC). Starting from the linear model as the baseline, a more complex model was accepted only if its AIC was lower by at least 2 units (Burnham et al., 2002). Because AIC is appropriate for comparing non-nested models, nested F-tests were run alongside as a check on whether the quadratic and piecewise models significantly reduced residual variance relative to the linear model.

Because the balance between energy limitation and water limitation shifts systematically with latitude, which may alter the position of breakpoints or the curvature of the response, the above analysis was repeated independently for three 10°-wide latitude bands (45–55°N, 55–65°N, 65–75°N) to test whether the shape of the temperature–ET response varies along the latitudinal temperature gradient.

An important trade-off applies to the anomaly framework. While anomaly computation effectively removes spatial gradient confounding, it also removes information about absolute temperature levels, which are central to the physical threshold mechanism tested in H2. A given temperature anomaly of +5°C corresponds to very different absolute temperatures across the latitudinal range, and the framework therefore conflates pixels that are physically far from any thermal threshold with those approaching it. The latitude-band stratification adopted in Section 5.2.2 partially addresses this limitation, but does not fully resolve it.

4.3.3 Partial Correlation Analysis of Dominant ET Drivers (H3)

The independent contributions of LST, LAI, Precip, SM and surface albedo to ET variability were quantified through a pixel-wise partial correlation analysis. The five drivers span the energy side (LST, Albedo), the water side (SM, Precip), and vegetation state (LAI). They covary in space and time, so partial correlation is used to isolate each driver's net association with ET after the other four are controlled for. Because these drivers covary in both space and time, simple bivariate correlations cannot distinguish their independent effects. Partial correlation isolates the net association of a target driver with ET after the remaining four candidates are linearly removed from both sides.

All input fields were placed on the common 0.1° grid defined in Section 4.1. The 0.05° MODIS-aligned LST, LAI, Albedo, FLUXCOM-X-BASE ET, and GLEAM v4.2a ET fields were upscaled to 0.1° using block-averaging. ERA5-Land SM and Precip were used at their native 0.1° resolution. The dry–wet ecosystem mask was reprojected from GLWD v2.0 onto the same 0.1° grid by computing the wet-pixel fraction within each 0.1° cell and classifying the cell as wet when the wet fraction reached or exceeded 0.5.The analysis was based on monthly anomaly series of each variable. For each pixel, a climatological mean was calculated for each calendar month (May–September) over 2001–2020. Each observation was then expressed as a departure from its corresponding monthly mean. This produced a 100-step anomaly series per pixel, one value for each month across the 20-year record.

The analysis was performed on monthly anomaly series. For each pixel and each calendar month (May–September), a 20-year climatology was computed for ET and for each of the five drivers, and each observation was expressed as a departure from its corresponding monthly mean. This produced 100-step anomaly series per pixel (20 years × 5 months) for all seven variables.

Taking the ET–LST partial correlation as an example, with LAI, Albedo, SM, and Precip serving as control variables, the procedure was as follows:

1. Regress the ET anomaly on the four control anomalies using ordinary least squares (OLS). The residuals from this regression, labelled *Y,* capture the part of ET variation that the four controls alone cannot explain.
2. Regress the LST anomaly on the same four controls using OLS, and extract the residuals *X*.
3. Compute the Pearson correlation coefficient between *eY* and , which is the partial correlation coefficient partial.

The same procedure was applied with each of the other four drivers as the target, the remaining four serving as controls. Pixels with fewer than 20 jointly valid (non-missing across ET and all five drivers) monthly observations were flagged as invalid. The statistical significance of each partial correlation coefficient was assessed using a t-test:

$$t = r_{partial}\sqrt{\frac{n-k-2}{1-r^2_{partial}}}$$

where n is the number of valid observations and k = 2 is the number of control variables. Two-tailed p-values were derived from the t-distribution with n − k − 2 degrees of freedom, with significance defined at $p < 0.05$. On this basis, for each pixel the driver with the largest absolute partial correlation coefficient that also passed the significance test was identified as the dominant driver of that pixel. Pixels where no driver passed the significance test were labelled as having no significant driver. Results were stratified by dry and wet ecosystems and, within each ecosystem class, by latitude band (45–55°N, 55–65°N, 65–75°N).

The analysis was repeated with GLEAM v4.2a in place of FLUXCOM-X-BASE, holding all other inputs identical, so any differences reflect the choice of ET product rather than the pipeline.

5 Results

5.1 H1: ET Partitioning in Dry vs. Wet Ecosystems under Greening

5.1.1 Greening Trends across Northern High Latitudes (>45°N)

The spatial distribution of summer (MJJAS) LAI over 2001–2020 reveals widespread vegetation greening across the high-latitude region north of 45°N (Fig. 5.1a). Strong greening signals are concentrated in southern Scandinavia, the East European Plain, the northern West Siberian Plain, the southern margins of the East Siberian Plateau, and southern Canada. Browning occurs mainly in eastern Siberia and along the North American Arctic coastline, but does not form spatially continuous patterns.

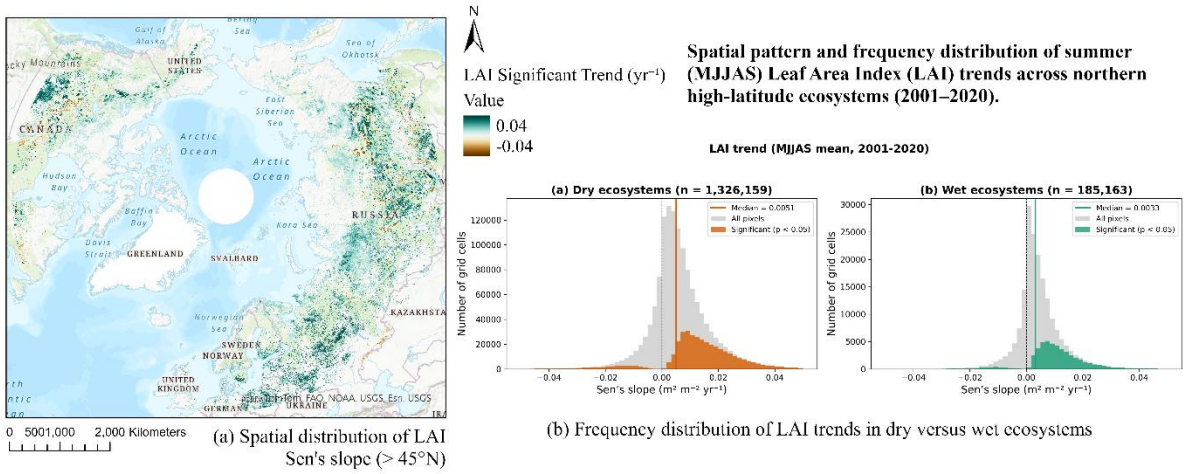

Figure 5.1 Spatial distribution and frequency distribution of summer (MJJAS) leaf area index (LAI) trends across northern high-latitude ecosystems (>45°N) during 2001–2020. (a) Pixel-wise Sen's slope of LAI (yr^{-1}) mapped in Arctic Polar Stereographic projection; only pixels with statistically significant trends (Mann-Kendall, $p < 0.05$) are shown in colour. (b) Frequency distributions of Sen's slope for dry ecosystems (n = 1,326,159) and wet ecosystems (n = 185,163); orange and teal bars indicate significant pixels ($p < 0.05$); dashed lines mark the median trend.

Dry ecosystems (n = 1,326,159) exhibit a median LAI trend of +0.0051 $m^2\ m^{-2}\ yr^{-1}$, compared with +0.0033 $m^2\ m^{-2}\ yr^{-1}$ for wet ecosystems (n = 185,163) (Fig. 5.1b). In both ecosystem types, roughly 25–26% of pixels show statistically significant greening ($p < 0.05$). Significant browning is far less common, affecting only 2–3% of pixels.

5.1.2 ∂ET/∂LAI Sensitivity

To quantify the influence of vegetation greening on evapotranspiration, all pixels were grouped into equal-count bins by climatological LAI, and the regression slope of ET trend against LAI

trend (∂ET/∂LAI) was computed within each bin. Both ecosystem types show a clear "L-shaped" decay of sensitivity with increasing LAI (Fig. 5.2b).

In dry ecosystems, sensitivity starts high: the lowest-LAI bin (around 0.2 m^2 m^{-2}) yields a ∂ET/∂LAI of roughly 35 mm $month^{-1}$ per unit LAI. It drops sharply to about 17 at LAI ≈ 0.7, then eases off gradually, settling at 8–10 beyond LAI ≈ 2.5. Wet ecosystems follow the same general shape, but the curve starts higher — nearly 1.5 times the dry-ecosystem value at comparable LAI levels. From there it falls quickly to around 18 at LAI ≈ 0.7 and flattens out at 11–13 once LAI exceeds 1.5.

The spatial map of ∂ET/∂LAI tells the same story from a different angle (Fig. 5.2a). High-sensitivity areas (∂ET/∂LAI > 20) sit in high-latitude tundra and sparse shrubland where climatological LAI stays below 0.7 — northern Siberia, the southern margins of the Canadian Arctic Archipelago, and the Hudson Bay region all fall into this category. Between LAI 0.7 and 1.5, marked by the black and green contour lines on the map, sensitivity drops to intermediate levels (12-20). In regions where LAI exceeds 1.5, such as central and southern Scandinavia, the southern West Siberian Plain, and the Canadian boreal forest belt, sensitivity falls broadly into the saturation range (blue, <8). In these areas, additional greening adds very little to total ET. This pattern of declining sensitivity at high LAI is consistent with the saturation effect documented in cross-ecosystem analyses (L. Wang et al., 2014; Yang et al., 2023).

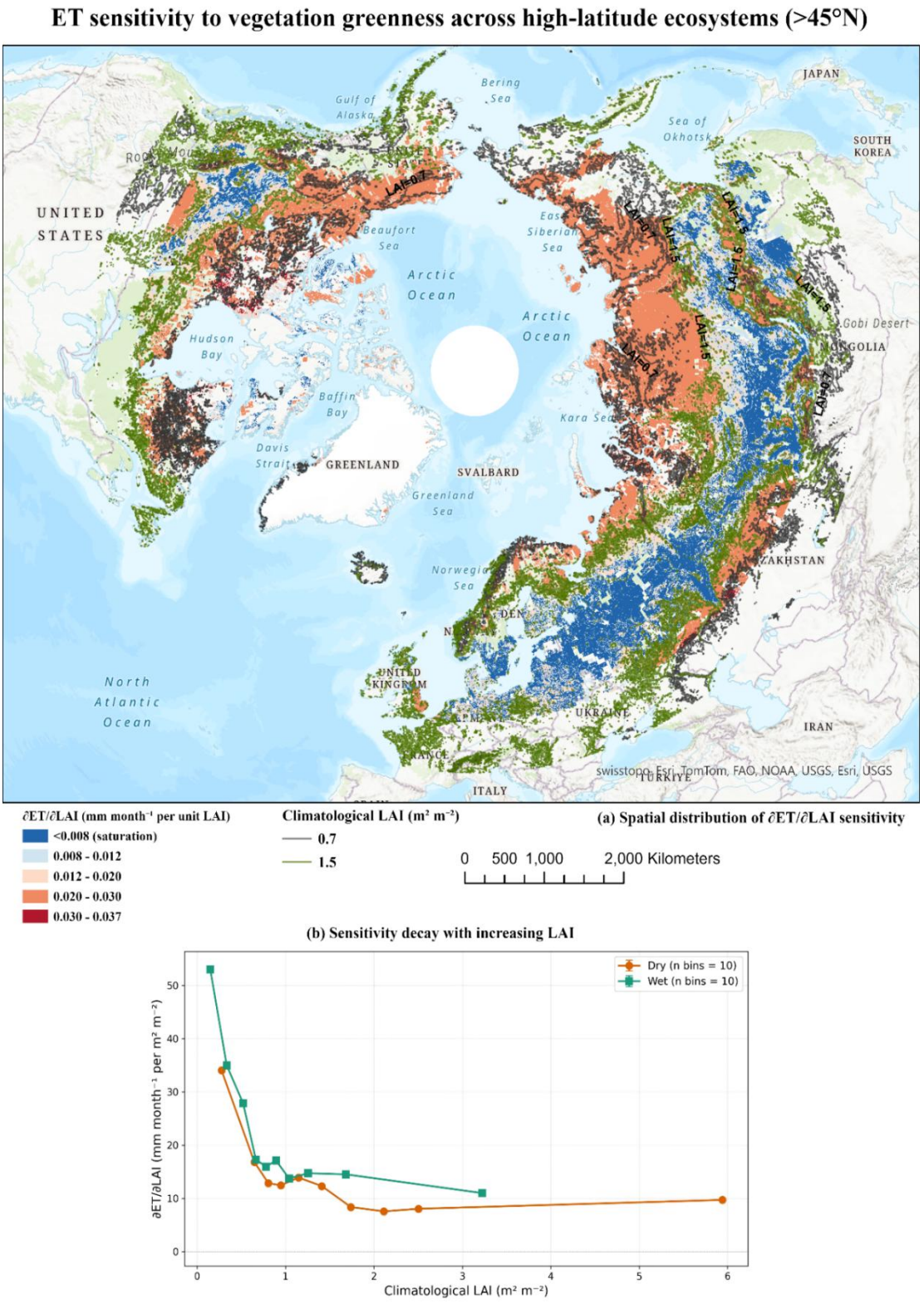

Figure 5.2 ET sensitivity to vegetation greenness across high-latitude ecosystems (>45°N). (a) Spatial distribution of pixel-wise partial regression coefficient ∂ET/∂LAI (mm month⁻¹ per unit LAI); blue pixels indicate climatological LAI above the saturation threshold (≥ 0.7 and 1.5 m² m⁻², contours shown); dark grey pixels are non-significant or unclassified. (b) Binned relationship between climatological mean LAI and ∂ET/∂LAI sensitivity for dry (orange) and wet (teal) ecosystems (10 bins each); values are the within-bin OLS regression of ET trend on LAI trend.

5.1.3 ET Component Substitution

Trends in transpiration fraction (Ec/ET) and bare-soil evaporation fraction (Es/ET) look very different between dry and wet ecosystems (Fig. 5.3).

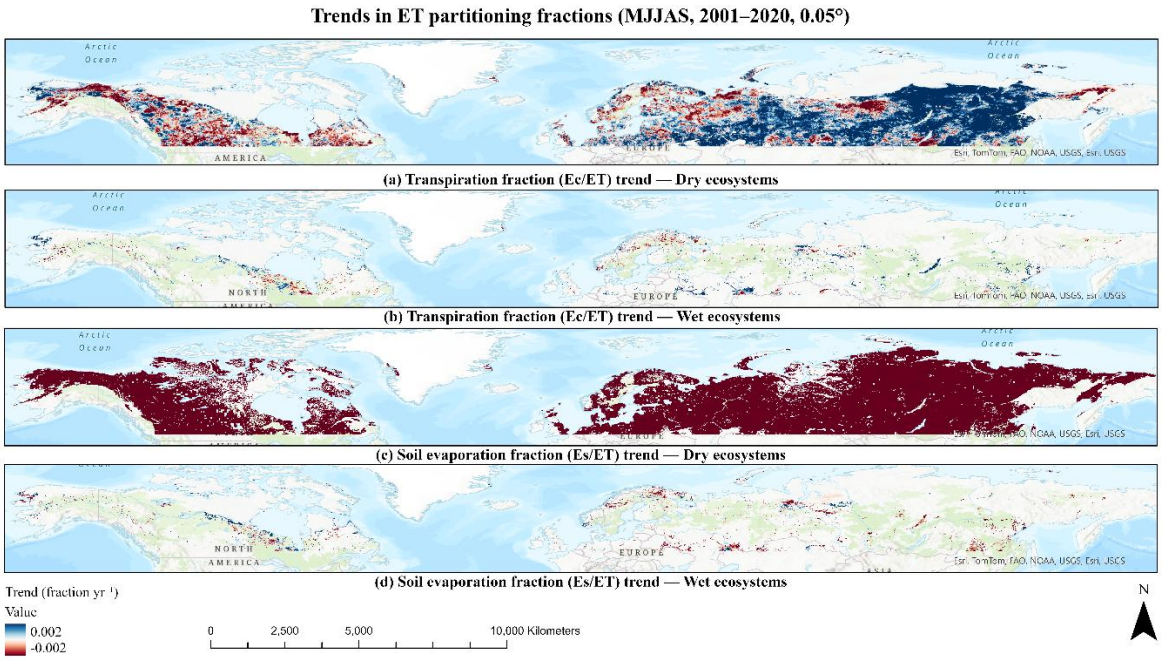

Figure 5.3 Spatial patterns of trends in ET partitioning fractions across northern high-latitude ecosystems (MJJAS, 2001–2020, 0.05° resolution). (a) Transpiration fraction (Ec/ET) trend — dry ecosystems. (b) Transpiration fraction (Ec/ET) trend — wet ecosystems. (c) Soil evaporation fraction (Es/ET) trend — dry ecosystems. (d) Soil evaporation fraction (Es/ET) trend — wet ecosystems. Colour scale indicates Sen's slope (fraction yr^{-1}); only pixels passing significance criteria are displayed.

In dry ecosystems, Ec/ET has increased across large, spatially connected areas — Siberia stand out most clearly (Fig. 5.3a). Es/ET in the same regions has moved in the opposite direction, with negative trends that map almost exactly onto the Ec/ET increases (Fig. 5.3c). Dry North America is less consistent, with increasing and decreasing trends mixed across the landscape.

Wet ecosystems tell a different story. Ec/ET trends are patchy and show no clear dominant direction (Fig. 5.3b). Es/ET covers limited area and the signal is weak throughout (Fig. 5.3d).

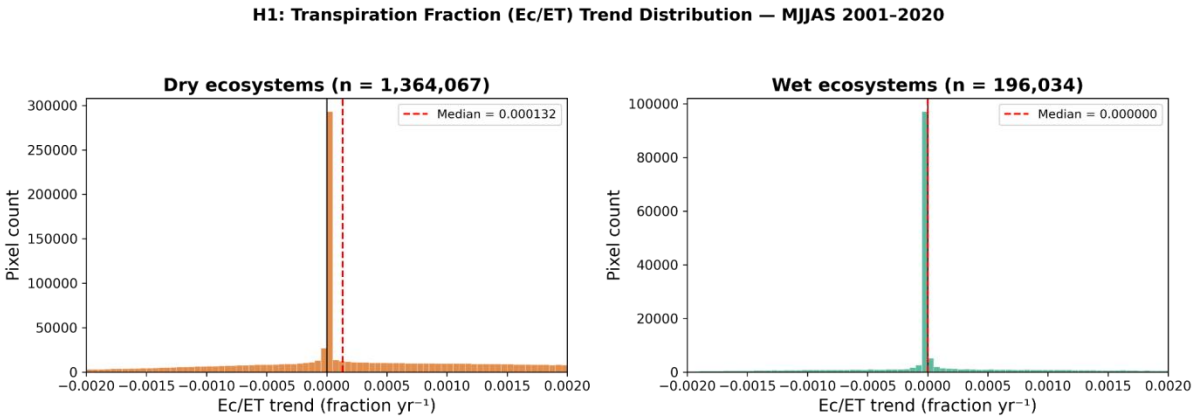

Figure 5.4 Frequency distributions of pixel-wise Sen's slope for the transpiration fraction (Ec/ET) trend across northern high-latitude ecosystems (MJJAS, 2001–2020). Dry ecosystems (n = 1,364,067) and wet ecosystems (n = 196,034) are shown separately. Dashed lines indicate the median Sen's slope for each ecosystem type (dry: +0.000132 fraction yr^{-1}; wet: 0.000000 fraction yr^{-1}).

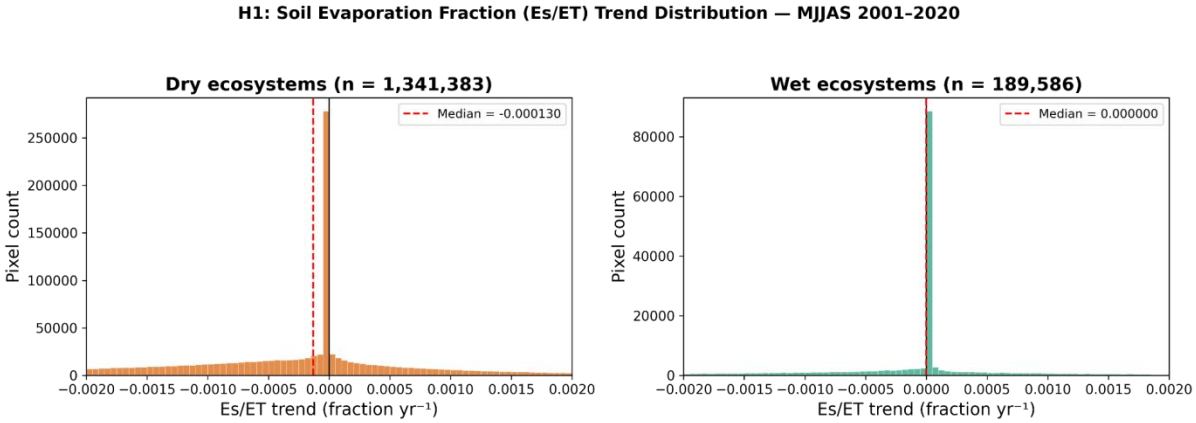

Figure 5.5 Frequency distributions of pixel-wise Sen's slope for the soil evaporation fraction (Es/ET) trend across northern high-latitude ecosystems (MJJAS, 2001–2020). Dry ecosystems (n = 1,341,383) and wet ecosystems (n = 189,586) are shown separately. Dashed lines indicate the median Sen's slope for each ecosystem type (dry: −0.000130 fraction yr^{-1}; wet: 0.000000 fraction yr^{-1}).

The statistical characteristics of the trend distributions further corroborate these spatial patterns (Fig. 5.5). The median Ec/ET trend in dry ecosystems is +0.000132 fraction yr^{-1}, while the median Es/ET trend is −0.000130 fraction yr^{-1} and the median Ei/ET trend is 0.000000 fraction yr^{-1} (Table 5.1). This proves that, within the ET budget of dry ecosystems, the increase in the transpiration share nearly exactly equals the decrease in the bare-soil evaporation share, with interception loss showing no detectable trend. In wet ecosystems, the median trends of all three fractions (Ec/ET, Es/ET, and Ei/ET) are 0.000000, with no detectable change in component structure. These distributions confirm that in dry ecosystems, the increase in transpiration share is almost exactly offset by the decrease in soil evaporation share, whereas wet ecosystems exhibit no detectable shift in either component fraction.

Table 5.1 Mass-balance closure diagnostic of GLEAM v4.2a component trends (MJJAS, 2001–2020). All values are pixel-wise medians of Theil–Sen slopes computed on the same grid. The closure residual r is defined as r = slope(Ec/ET) + slope(Es/ET) + slope(Ei/ET).

Ecosystem	n	Median Ec/ET (yr^{-1})	Median Es/ET (yr^{-1})	Median Ei/ET (yr^{-1})	Sum (yr^{-1})	Median |r|	P95 |r|
Dry	1,339,59	+0.0001323	−0.0001301	+0.000000	+0.0000022	0.000364	0.0037097
Wet	188,938	+0.0000000	+0.0000000	+0.000000	+0.0000000	0.000091	0.0033235

5.1.4 Relationship between LAI and Ec/ET

Pixel-level linear regressions were performed between LAI trends and Ec/ET trends (Fig. 5.6).

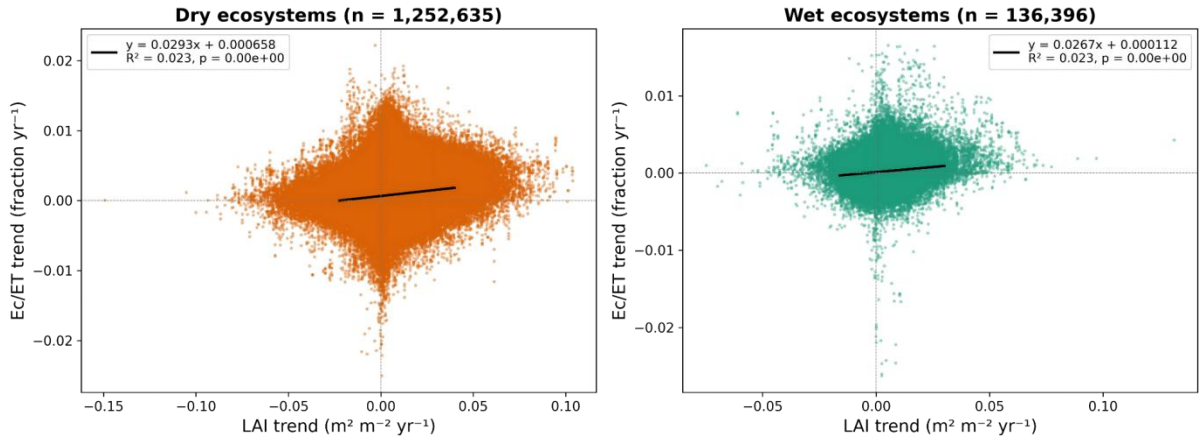

Figure 5.6 Pixel-level relationship between summer (MJJAS) LAI trend and transpiration fraction (Ec/ET) trend across northern high-latitude ecosystems (2001–2020). Dry ecosystems (n = 1,252,635) and wet ecosystems (n = 136,396) are shown separately. Black lines indicate ordinary least-squares regression fits; regression equations and coefficients of determination (R^2) are given in each panel.

In both ecosystem types, LAI trends and Ec/ET trends are significantly positively correlated ($p \approx 0$): the regression slope is 0.0293 for dry ecosystems and 0.0267 for wet ecosystems, indicating that the magnitude of Ec/ET increase associated with each unit increase in greening is similar between the two. However, R^2 is only 0.023 in both cases, indicating that LAI trends account for approximately 2% of the variance in Ec/ET trends. At this level of explained variance, the regression establishes the sign and the upper-bound scaling of the LAI–Ec/ET relationship, but does not establish LAI trends as the quantitative dominant control on the spatial variability of the Ec/ET trend.

The meaning of the intercept is the expected Ec/ET trend when the LAI trend is zero, representing the rate at which Ec/ET increases even in the absence of greening. The regression intercept for dry ecosystems is +0.000658, far exceeding the +0.000112 for wet ecosystems, indicating that dry ecosystems exhibit a baseline Ec/ET increase independent of vegetation greening, roughly six times the magnitude of that in wet ecosystems. A direct comparison of magnitudes makes the asymmetry between the two terms explicit: in dry ecosystems, the LAI-driven contribution evaluated at the median greening rate is slope × median LAI trend = 0.0293 × 0.0051 ≈ +0.000149 fraction yr^{-1}, which is only about 23% of the LAI-independent intercept (+0.000658 fraction yr^{-1}). Even at the median greening rate, the bulk of the dry-ecosystem Ec/ET trend is therefore attributable to processes operating independently of LAI change. Other candidate drivers will be further examined through partial correlation analysis in H3.

5.1.5 Consistency in Total ET Trends between FLUXCOM-X-BASE and GLEAM v4.2a

In both products, the median MJJAS total ET slope was positive in dry and wet ecosystems, and the direction was fully consistent (Table 5.2). In dry ecosystems, the median slopes from FLUXCOM and GLEAM were +0.121 and +0.114 mm $month^{-1}$ yr^{-1}, respectively, corresponding to a relative difference of approximately 6.2%; in wet ecosystems, the median slopes from both products were +0.092 mm $month^{-1}$ yr^{-1}, with a difference below 0.01%. The mean slopes showed comparable consistency: in dry ecosystems, FLUXCOM and GLEAM yielded +0.121 and +0.122 mm $month^{-1}$ yr^{-1} (a difference of approximately 1%), while in wet ecosystems they yielded +0.091 and +0.081 (a difference of approximately 11%). With respect to the proportion of pixels with a significant positive trend, FLUXCOM gave 18.7% and 15.7% for dry and wet ecosystems, respectively, while GLEAM gave 14.8% and 7.3%. The proportion of pixels with a significant negative trend was between 1.2% and 1.6% in both products, with negligible differences.

Table 5.2 Comparison of MJJAS total ET trend statistics (2001–2020) between FLUXCOM-X-BASE and GLEAM v4.2a in dry and wet ecosystems. FLUXCOM values have been converted from native mm hr^{-1} to mm $month^{-1}$.

Metric	FLUXCOM DRY	GLEAM DRY	FLUXCOM WET	GLEAM WET
Number of pixels (n)	1,438,495	1,567,681	213,923	215,797
Median slope (mm $month^{-1}$ yr^{-1})	0.120798	0.113779	0.091702	0.091701
Mean slope (mm $month^{-1}$ yr^{-1})	0.121231	0.12242	0.090639	0.080759
Q25 (mm $month^{-1}$ yr^{-1})	0.025336	-0.001763	0.018124	-0.016495
Q75 (mm $month^{-1}$ yr^{-1})	0.216319	0.249173	0.175986	0.198669
Significant positive trend (%)	18.7	14.8	15.7	7.3
Significant negative trend (%)	1.6	1.4	1.3	1.2
Non-significant (%)	79.7	83.8	83	91.5
Interannual anomaly Pearson r	$r = +0.915$ ($p = 1.6 \times 10^{-8}$)		$r = +0.822$ ($p = 8.9 \times 10^{-6}$)	

When the regional-mean interannual MJJAS ET anomalies were plotted as time series (Fig. 5.7), the two products exhibited highly synchronous fluctuations in both dry and wet ecosystems. The Pearson correlation coefficient of the interannual anomalies was +0.915 in dry ecosystems ($p = 1.6 \times 10^{-8}$) and +0.822 in wet ecosystems ($p = 8.9 \times 10^{-6}$). The regression trend lines of the two products were nearly parallel, and the low-anomaly years of 2004, 2008, 2010, and 2019, as well as the high-anomaly years of 2011, 2013, 2016, and 2020, were identifiable in both curves. A discrepancy was found in the magnitude of the 2001–2020 multi-year MJJAS mean ET between FLUXCOM and GLEAM: in dry ecosystems, FLUXCOM gave 45.69 mm $month^{-1}$ and GLEAM 53.49 mm $month^{-1}$; in wet ecosystems, FLUXCOM gave 36.03 mm $month^{-1}$ and GLEAM 48.35 mm $month^{-1}$. FLUXCOM was lower than GLEAM by 14.6% in dry ecosystems and by 25.5% in wet ecosystems.

The most prominent residual difference between the two products was in the proportion of pixels with a significant positive trend in wet ecosystems: 7.3% in GLEAM, markedly lower than 15.7% in FLUXCOM, while the corresponding difference in dry ecosystems (14.8% versus 18.7%) was comparatively smaller. In addition, the slope distribution of GLEAM was slightly broader than that of FLUXCOM in both ecosystem types, and the first quartile (Q25)

was closer to 0 than in FLUXCOM (for example, Q25 = −0.002 mm month^{-1} yr^{-1} in GLEAM dry ecosystems, compared with +0.025 mm month^{-1} yr^{-1} in FLUXCOM).

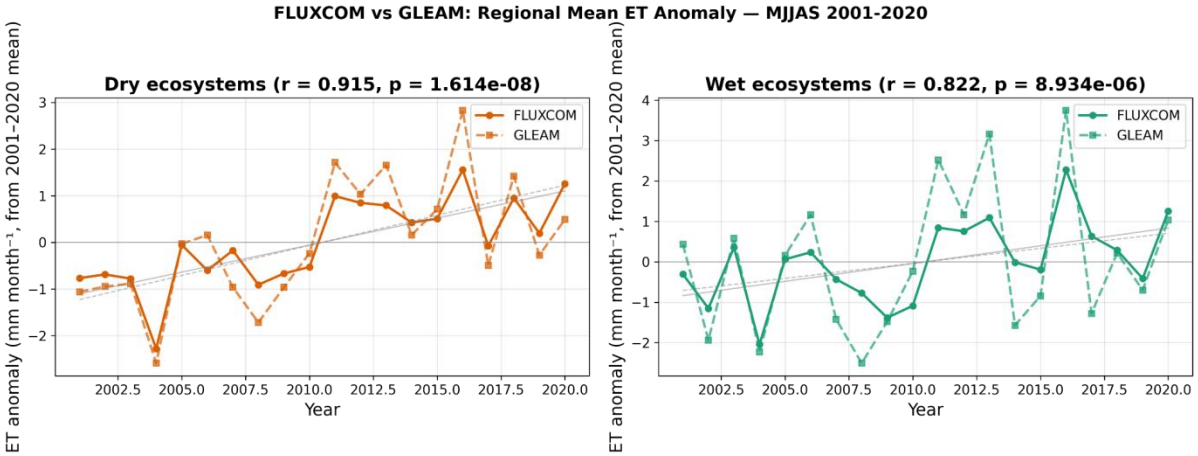

Figure 5.7 Interannual time series of regional-mean MJJAS ET anomalies from FLUXCOM-X-BASE and GLEAM v4.2a (2001–2020). Left: dry ecosystems; right: wet ecosystems. Anomalies are computed relative to each product's own 2001–2020 multi-year mean. Solid lines (orange/green, circles) denote FLUXCOM; dashed lines (light tones, squares) denote GLEAM; thin grey lines indicate the corresponding linear regression trends. Pearson correlation coefficients and p-values shown in the subplot titles quantify the interannual synchrony between the two products in each ecosystem type.

5.2 H2: Temperature–ET Non-linearity

5.2.1 Anomaly Response

Monthly anomalies (ΔLST, ΔET) for all pixels across the study domain were binned and fitted with three competing models: linear, quadratic, and piecewise linear, with R^2 as the model selection criterion (Fig. 5.8). Dry ecosystems contributed roughly 99.9 million pixel-month observations, and wet ecosystems approximately 13.5 million. Across both ecosystem types, ΔET barely responds to temperature when ΔLST drops below around −9°C, but rises steeply once that threshold is passed. The piecewise linear model fits best in both cases (dry $R^2 = 0.894$; wet $R^2 = 0.945$), ahead of both the linear and quadratic alternatives.

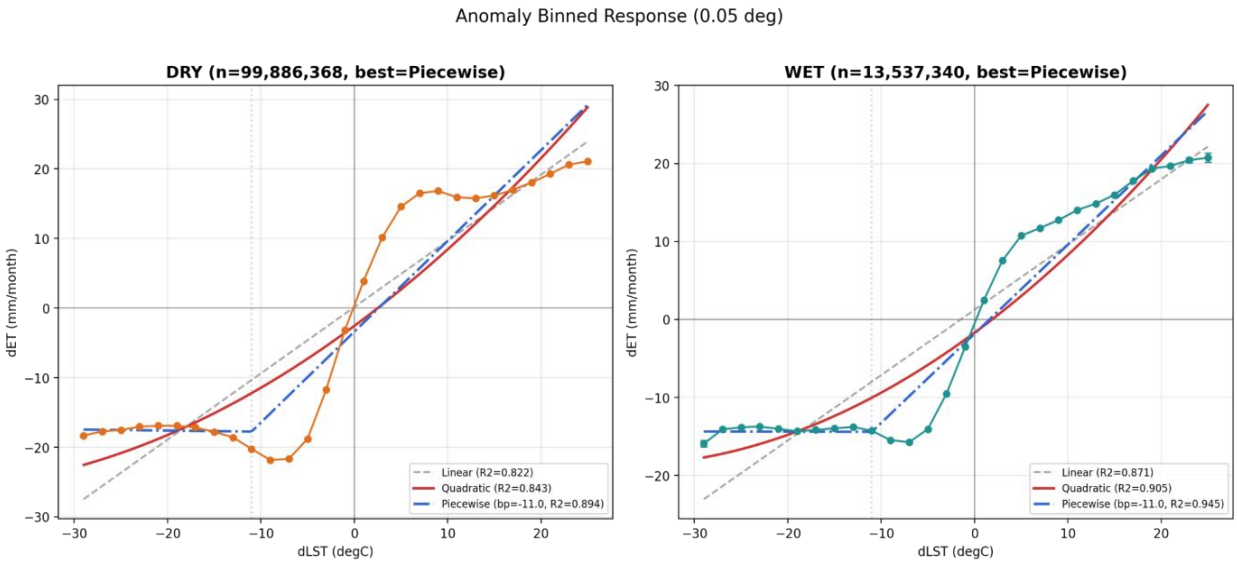

Figure 5.8 Binned ΔLST–ΔET anomaly response curves and model fits for dry and wet ecosystems across northern high-latitude regions (MJJAS, 2001–2020, 0.05° resolution). Pixel-month anomaly pairs were aggregated into equal-frequency bins; markers show bin means. Three competing models are fitted to each ecosystem type: linear (dashed grey), quadratic (red), and piecewise linear (blue). Best-fit model selected by R^2; breakpoint (bp) and R^2 values are annotated for the piecewise model. Dry: n = 99,886,368; Wet: n = 13,537,340.

The breakpoint reflects a cold-end physiological constraint rather than a warm-end water-limitation threshold. When temperature anomalies fall below this breakpoint, most pixels are under snow or ice, or vegetation has gone dormant. ET has already reached its physical lower limit, so further cooling no longer causes additional ET decline. Above the breakpoint, rising temperature drives ET up by increasing atmospheric evaporative demand and waking vegetation out of dormancy.

The scatter density plot (Fig. 5.8) shows that observations with ΔLST above +10°C are very sparse in dry ecosystems. Bin means in that range rest on too few data points to say anything reliable. The domain-wide analysis therefore cannot test H2, which is specifically about warm-end water limitation. What this analysis captures is the cold-end physics of snow cover and dormancy, which is a separate question entirely. The analysis is therefore repeated by latitude band in Section 5.2.2 to isolate the warm-end signal of interest.

5.2.2 Temperature–ET Response by Latitude Band

Although the domain-wide analysis did not detect warm-end divergence between dry and wet ecosystems, latitude-band stratification reveals a latitudinal gradient in the temperature–ET response (Fig. 5.9). In the 65–75°N band, the piecewise model is optimal for both dry (R^2 = 0.957, bp = −10.0°C) and wet (R^2 = 0.990, bp = −8.0°C) ecosystems. Both exhibit a cold-end plateau below approximately −9°C. However, above the breakpoint, the responses of dry and wet ecosystems begin to diverge: wet bin means continue to increase steadily above the breakpoint, fitting the piecewise model well, whereas dry ecosystems enter a plateau after ΔLST > +10°C, with growth notably slowing and bin means no longer following the fitted line. This divergence indicates that even at high latitudes, dry ecosystems already show signs of ET

response saturation at large positive temperature anomalies, while wet ecosystems, with sufficient water supply, continue to increase monotonically.

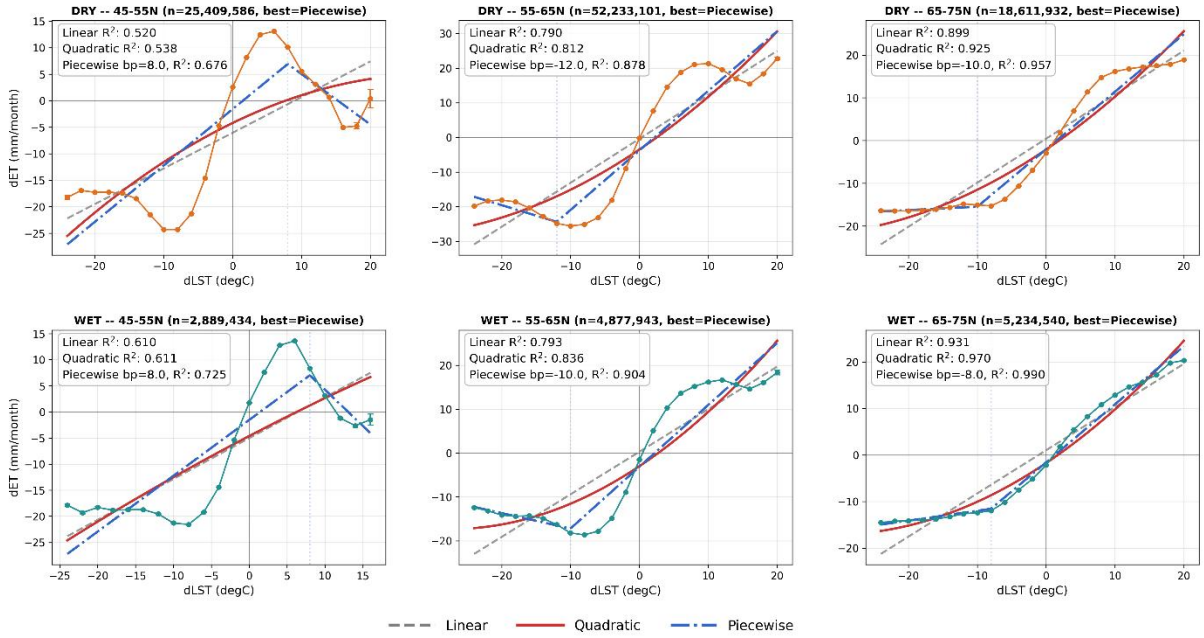

Figure 5.9 Latitudinal stratification of the ΔLST–ΔET anomaly response across three latitude bands (45–55°N, 55–65°N, 65–75°N) for dry (orange, upper row) and wet (teal, lower row) ecosystems (MJJAS, 2001–2020). Markers show bin means; fitted curves follow the same convention as Figure 5.8. Piecewise breakpoint (bp) and R^2 are annotated for each panel. Sample sizes (n) are given in panel titles.

In the 55–65°N band, both ecosystem types retain the hockey-stick structure seen at higher latitudes, with breakpoints anchored at the cold end. Above the breakpoint, dry ecosystem bin means track the fitted line reasonably well until ΔLST exceeds roughly +15°C, where a modest downturn appears. Wet ecosystems are less sensitive at the warm end; bin means scatter somewhat in the final bins but do not depart from the upward trend.

In the 45–55°N band, the response pattern has a different shift. For dry ecosystems, the breakpoint shifts to the warm end (bp = +8.0°C), and bin means peak near ΔLST ≈ +5–8°C before declining, forming an inverted-U pattern that suggests ET begins to fall off once positive temperature anomalies grow large enough. Wet ecosystems follow a structurally similar change: R^2 drops to 0.725, the breakpoint lands at the same +8.0°C threshold, and bin means become increasingly erratic before turning downward at the warm end. That both ecosystem types converge on the same breakpoint location points to a shared constraint, most likely a transition from energy-limited to water-limited conditions, becoming active across this latitude band.

Moving southward, the warm-end suppression appears to deepen rather than diminish, suggesting that 45–55°N marks the northern edge of a thermal sensitivity gradient rather than an isolated anomaly. Within this band, the inverted-U shows up in both dry and wet pixels, though dry ecosystems show a steeper downturn, consistent with their tighter coupling to water availability.

5.2.3 Spatial Context of Growing Season Temperature

The spatial distribution of mean growing season LST supports the latitude-band stratification results (Fig. 5.10). The 15°C and 20°C isotherms together divide the study domain into three temperature zones, each corresponding to a distinct response pattern identified in the piecewise analysis. Across the high-latitude over 65°N, growing season temperatures fall largely below 5°C and drop below −5°C over extensive areas, placing these regions within the cold-limited conditions of the 65–75°N band where both ecosystem types maintain an increasing ET response throughout the observed temperature range. The 15°C isotherm runs approximately along 55–60°N; the broad belt north of it aligns with the latitude bands where warm-end suppression has not yet emerged. South of the 20°C isotherm, the map shifts to orange-red and deep red tones, reflecting the warm-end ET suppression signal detected in the 45–55°N band. These areas cover Central Asia, the southern East European Plain, southern Siberia, and the North American Great Plains. Wet ecosystems cluster north of the 15°C isotherm, spanning the Western Siberian Lowlands, the Hudson Bay Lowlands, the Canadian Shield, and northern Scandinavia. The regions south of the 20°C isotherm, by contrast, fall largely within the 45–55°N band and overlap with areas where the warm-end decline is observed in the binned response.

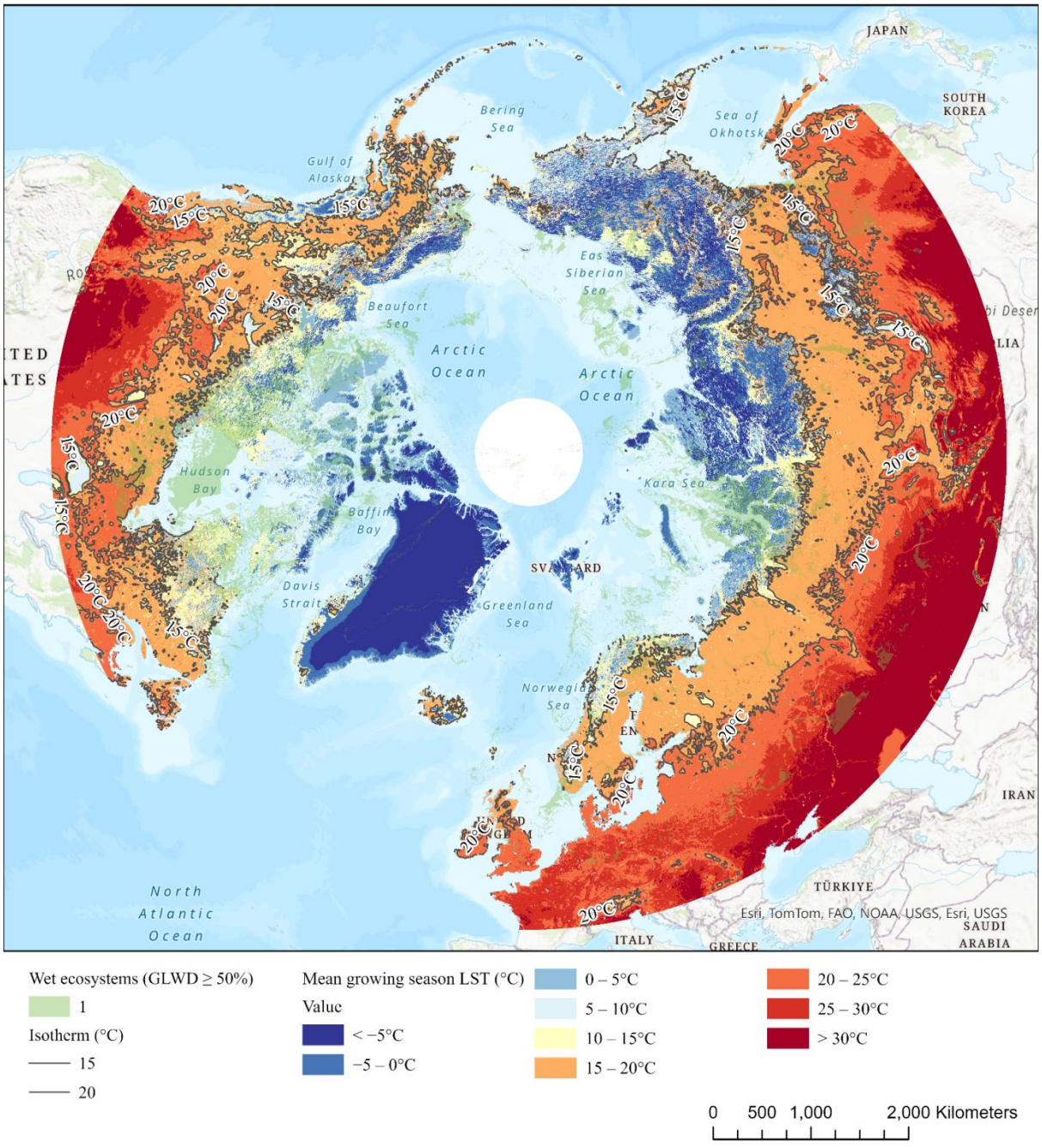

Figure 5.10 Spatial distribution of mean growing season land surface temperature (LST; MJJAS, 2001–2020) across the study domain (>45°N). Wet ecosystem extent (GLWD ≥ 50%; teal outline) and 15°C/20°C isotherms (grey contours) are overlaid; the isotherms delineate the temperature range associated with the warm-end ET peak detected in dry ecosystems at 45–55°N.

5.3 H3: Driver Attribution across Dry and Wet Ecosystems

5.3.1 Different Domain-wide Drivers

Median pixel-wise partial correlations between ET anomalies and the five candidate drivers are summarised in Table 5.3 and shown in Figure 5.11 for both ET products and both ecosystem classes.

LAI is the strongest positive partial correlate of ET anomalies in every product–ecosystem combination. Under FLUXCOM-X-BASE, the LAI median is +0.50 in dry pixels and +0.47 in wet pixels, with 93.0% and 85.5% of pixels respectively passing the $p < 0.05$ significance test. Under GLEAM v4.2a, the corresponding LAI medians are +0.27 (dry) and +0.24 (wet), although LAI retains the largest positive magnitude among the five drivers under both products. LST is the second strongest positive driver under both products, with medians clustered narrowly around +0.20 (FLUXCOM: +0.21 dry, +0.20 wet; GLEAM: +0.19 dry, +0.17 wet) and significance rates between 37.6% and 53.1%.

Table 5.3 Median and mean pixel-wise partial correlation coefficients between MJJAS monthly ET anomalies (2001–2020) and five candidate drivers — LST, LAI, surface albedo, soil moisture, and precipitation — for FLUXCOM-X-BASE and GLEAM v4.2a ET products in dry and wet ecosystems. *N* is the number of pixels included in each summary; "% sig" is the proportion of pixels whose partial correlation passes the *t*-test at $p < 0.05$.

Product	Ecosystem	Driver	Median r	Mean r	% sig	N
FLUXCOM	DRY	LST	0.2121	0.1896	53.14	287967
FLUXCOM	DRY	LAI	0.4989	0.491	93.05	287967
FLUXCOM	DRY	Albedo	0.0384	0.0287	19.92	287967
FLUXCOM	DRY	SM	-0.2137	-0.2049	50.98	286797
FLUXCOM	DRY	Precip	-0.206	-0.201	48.82	287967
FLUXCOM	WET	LST	0.204	0.1889	47.03	48526
FLUXCOM	WET	LAI	0.4717	0.4469	85.49	48523
FLUXCOM	WET	Albedo	-0.0242	-0.0315	20.79	48526
FLUXCOM	WET	SM	-0.306	-0.2838	69.6	48341
FLUXCOM	WET	Precip	-0.1405	-0.1509	31.47	48526
GLEAM	DRY	LST	0.1877	0.1828	44.16	287577
GLEAM	DRY	LAI	0.2706	0.2595	65.06	287568

Product	Ecosystem	Driver	Median r	Mean r	% sig	N
GLEAM	DRY	Albedo	-0.1045	-0.1141	31.28	287567
GLEAM	DRY	SM	-0.1873	-0.172	50.51	286413
GLEAM	DRY	Precip	-0.0983	-0.0942	21.56	287572
GLEAM	WET	LST	0.1727	0.1688	37.63	48389
GLEAM	WET	LAI	0.2381	0.2261	54.4	48388
GLEAM	WET	Albedo	-0.1274	-0.1349	30.95	48388
GLEAM	WET	SM	-0.2179	-0.2091	50.67	48202
GLEAM	WET	Precip	-0.0967	-0.0942	19.1	48388

The two water-related drivers, SM and Precip, return negative median partial correlations in every product–ecosystem combination. Under FLUXCOM-X-BASE, the SM median is −0.21 in dry pixels and −0.31 in wet pixels; the corresponding Precip values are −0.21 and −0.14. Under GLEAM, SM medians are −0.19 (dry) and −0.22 (wet), and Precip medians are −0.10 in both ecosystem classes. Albedo shows the weakest partial association, with medians ranging between −0.13 and +0.04.

The contrast between dry and wet ecosystems is small for every driver. The largest dry–wet gap in median partial correlation is observed for FLUXCOM SM (0.10 absolute units), followed by FLUXCOM Precip (0.07); all remaining product–driver combinations exhibit dry–wet gaps of 0.05 absolute units or less.

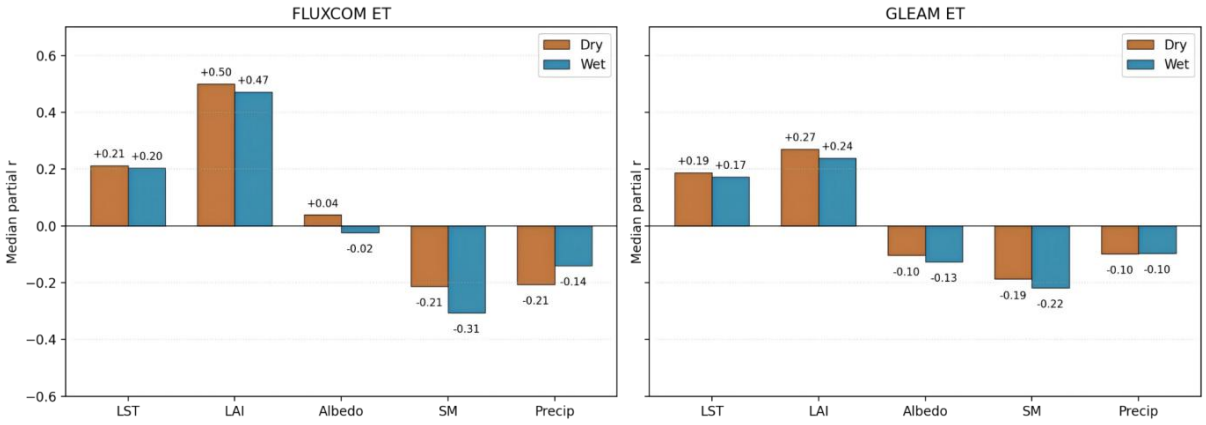

Figure 5.11 Median pixel-wise partial correlations between MJJAS monthly ET anomalies (2001–2020) and five candidate drivers — LST, LAI, Albedo, SM, and Precip — under (left) FLUXCOM-X-BASE and (right) GLEAM v4.2a ET products. Bars are colour-coded by ecosystem class (orange = dry; blue = wet). Numerical labels above or below each bar give the median value to two decimal places.

5.3.2 Latitudinal Strengthening of Soil Moisture and Temperature Signals

The partial correlations based on FLUXCOM-X-BASE were classified by three latitude bands (45–55°N, 55–65°N, 65–75°N) within each ecosystem (Figure 5.12).

The LST partial correlation strengthens with latitude under both ecosystem classes. The median rises from +0.10 (dry) and +0.12 (wet) in 45–55°N, to +0.23 and +0.20 in 55–65°N, and remains high at +0.24 and +0.22 in 65–75°N. In contrast, the SM partial correlation is consistently negative, but its absolute strength increases with latitude. The signed median shifts from −0.09 (dry) and −0.17 (wet) in 45–55°N, to −0.20 and −0.28 in 55–65°N, and further to −0.33 and −0.36 in 65–75°N. Thus, higher-latitude pixels show a stronger negative association between ET and SM after controlling for the other drivers, rather than a positive soil-moisture control. Albedo also shifts from positive to negative with latitude, with its median moving from +0.10 (dry) and +0.07 (wet) in 45–55°N to −0.06 and −0.13 in 65–75°N.

LAI and Precip show the opposite pattern. The LAI median remains close to +0.50 across the two lower latitude bands in both ecosystem classes, and weakens only in 65–75°N (+0.49 dry, +0.42 wet). The Precip absolute median is largest in the two lower bands, reaching 0.23 in dry pixels and 0.17–0.18 in wet pixels, but contracts in 65–75°N to 0.11 and 0.08, respectively.

Within each driver, the difference between the dry and wet medians is consistently smaller than the difference across latitude bands. For LST, the largest dry–wet gap in any single band is 0.03, whereas the median rises by 0.14–0.11 absolute units between 45–55°N and 65–75°N. For SM, the largest dry–wet gap in any single band is 0.08, whereas the median strengthens by 0.24 (dry) and 0.19 (wet) absolute units across the same latitudinal span. The strongest gradient in driver structure is therefore latitudinal rather than between dry and wet ecosystems.

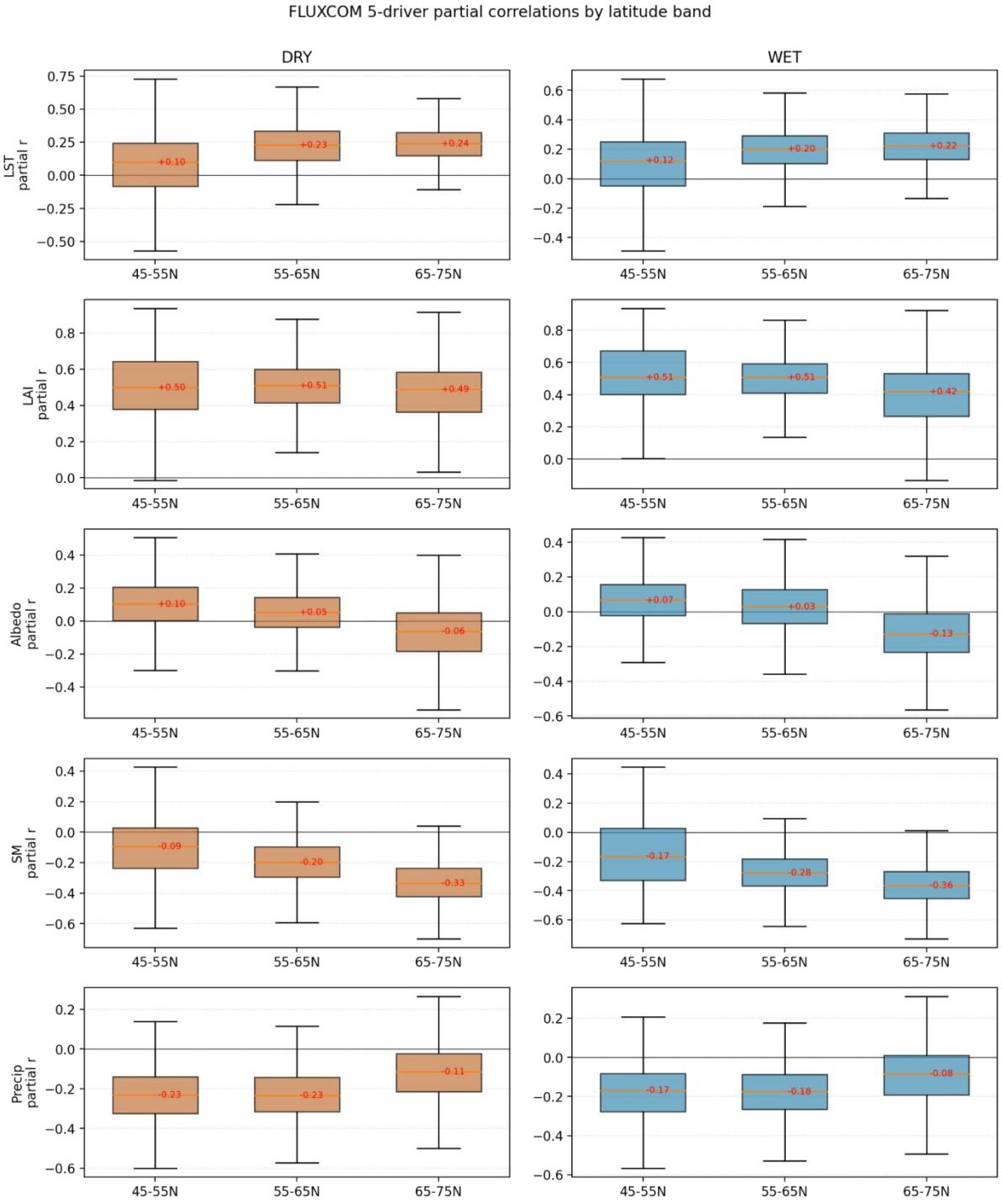

Figure 5.12 Box-and-whisker distributions of pixel-wise five-driver partial correlations between MJJAS monthly FLUXCOM-X-BASE ET anomalies (2001–2020) and LST, LAI, Albedo, SM, and Precip, stratified by latitude band (45–55°N, 55–65°N, 65–75°N) for (left) dry ecosystems and (right) wet ecosystems. Boxes show the interquartile range; whiskers extend to the 5th and 95th percentiles. Numerical labels give the median value to two decimal places.

5.3.3 Cross-Product Comparison of Dominant Drivers

Under FLUXCOM-X-BASE, LAI is the dominant driver of 75% of dry pixels and 65% of wet pixels (Figures 5.13, 5.14). Under GLEAM v4.2a, the same map breaks into coherent patches of LAI, SM, and LST, and the LAI share drops to 34% (dry) and 29% (wet).

The reorganisation under GLEAM is absorbed primarily by SM and LST. SM dominance rises from 9% to 26% in dry pixels and from 19% to 28% in wet pixels; LST dominance rises from 7% to 15% (dry) and from 6% to 13% (wet); and Albedo dominance rises from 2% to 13% (dry) and from 2% to 12% (wet). Precip dominance remains low under both products (5–8%). Pixels with no significant driver are negligible under FLUXCOM-X-BASE (1% in both ecosystem classes) but reach 7% (dry) and 12% (wet) under GLEAM v4.2a.

The LST median partial correlation is reproduced across products to within 0.04 absolute units in both ecosystem classes (Section 5.3.1), whereas the dominant-driver share of LAI is approximately halved between the two products. Cross-product stability therefore depends on which summary statistic is taken.

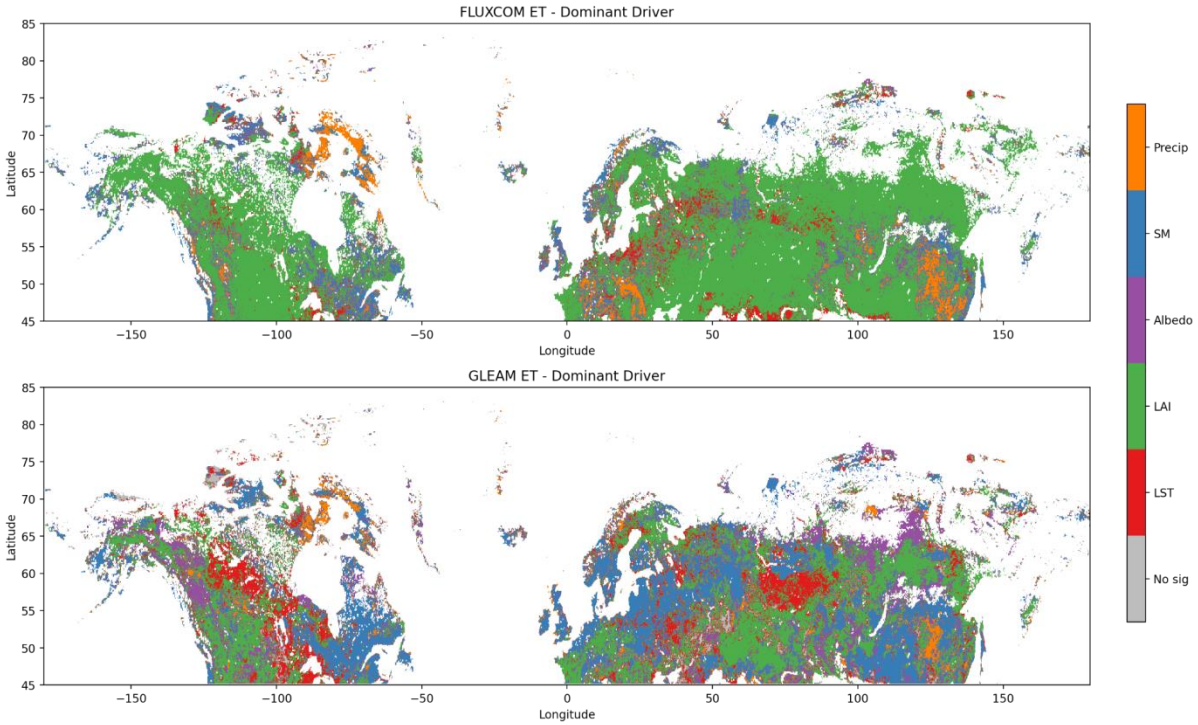

Figure 5.13 Pixel-wise dominant-driver classification under (top) FLUXCOM-X-BASE and (bottom) GLEAM v4.2a ET products for MJJAS 2001–2020. For each pixel, the driver with the largest absolute five-driver partial correlation passing the $p < 0.05$ significance test is shown. Grey indicates pixels in which no driver passed the significance test.

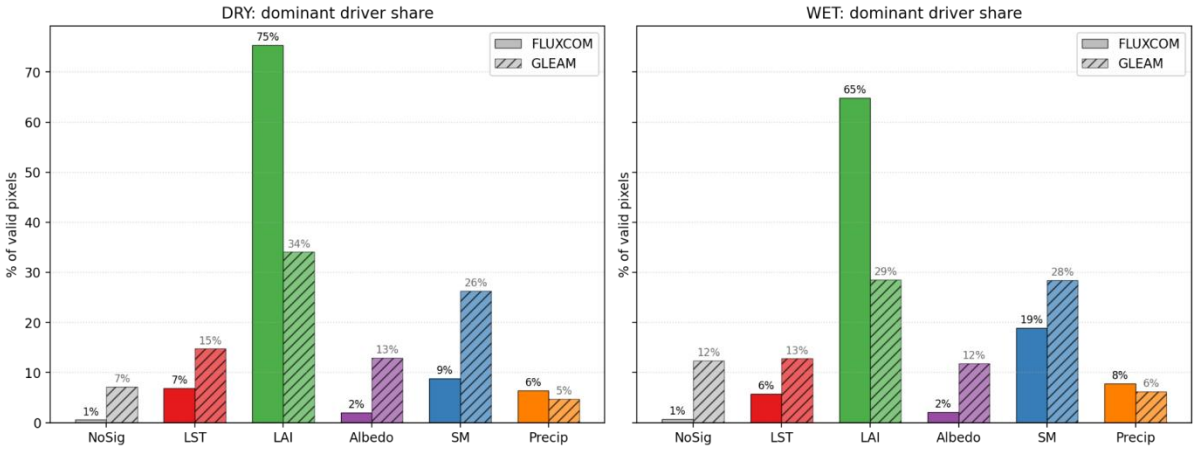

Figure 5.14 Dominant-driver share among valid pixels under FLUXCOM-X-BASE (solid bars) and GLEAM v4.2a (hatched bars) for (left) dry and (right) wet ecosystems. Numerical labels above each bar give the percentage of valid pixels assigned to the corresponding driver class.

5.3.4 Observed Patterns versus H3 Predictions

The four predictions stated in Section 2.2 are summarised against the observed median partial correlations and dominant-driver shares in Table 5.4.

Prediction (i) states that water-related drivers — SM and Precip — show partial correlations of larger absolute magnitude in dry pixels than in wet pixels. The SM median is larger in absolute magnitude in wet pixels than in dry pixels under FLUXCOM-X-BASE, and is of comparable magnitude under GLEAM v4.2a. The Precip median follows the predicted direction under FLUXCOM-X-BASE but is equal between dry and wet pixels under GLEAM v4.2a, at 0.10 in both.

Prediction (ii) states that LST shows a larger partial correlation in wet pixels than in dry pixels. The LST medians are nearly identical between dry and wet pixels under both products (FLUXCOM-X-BASE: +0.21 dry, +0.20 wet; GLEAM v4.2a: +0.19 dry, +0.17 wet), with a maximum dry–wet gap of 0.03 absolute units.

Prediction (iii) states that water-related drivers account for a larger share of dominant-driver pixels in dry ecosystems than in wet ecosystems. The SM-dominant share is larger in wet pixels than in dry pixels under both products. The Precip-dominant share is small under both products (5–8%) and shows no systematic dry–wet contrast.

Prediction (iv) states that the dry–wet contrasts identified under FLUXCOM-X-BASE are reproduced under GLEAM v4.2a. The LST median partial correlation is reproduced across products to within 0.04 absolute units in both ecosystem classes. The LAI-dominant share is approximately halved between the two products (FLUXCOM-X-BASE: 75% / 65%; GLEAM v4.2a: 34% / 29%).

The interpretation of these comparisons and their implications for H3 are taken up in Section 6.3.

Table 5.4 Summary of the four predictions stated in Section 2.2 against the observed median partial correlations and dominant-driver shares from Sections 5.3.1 and 5.3.3.

Prediction	Quantity	Predicted direction	FLUXCOM-X-BASE	GLEAM v4.2a
(i)	|SM median *r*|	dry > wet	wet > dry (0.31 vs 0.21)	wet ≈ dry (0.22 vs 0.19)
	|Precip median *r*|	dry > wet	dry > wet (0.21 vs 0.14)	dry = wet (0.10 vs 0.10)
(ii)	LST median *r*	wet > dry	dry ≈ wet (+0.21 vs +0.20)	dry ≈ wet (+0.19 vs +0.17)
(iii)	SM-dominant share	dry > wet	wet > dry (19% vs 9%)	wet > dry (28% vs 26%)
(iii)	Precip-dominant share	dry > wet	wet > dry (8% vs 6%)	dry ≈ wet (5% vs 6%)
(iv)	LST median *r*	reproduced across products	+0.21 / +0.20	+0.19 / +0.17
	LAI-dominant share	reproduced across products	75% / 65%	34% / 29%

6 Discussion

6.1 Mechanisms of ET Partitioning Reorganization in Dry and Wet Ecosystems

In dry ecosystems, total ET did not increase substantially. Instead, the increase in Ec/ET and the decrease in Es/ET showed an almost mirror-like relationship, whereas wet ecosystems did not exhibit a comparable component-level divergence. This contrast suggests that the core pattern behind H1 is not a straightforward expansion of total ET, but a systematic redistribution of the internal component structure of ET. In dry ecosystems, this shift is better understood as an energy redistribution process than as a direct consequence of LAI growth driving stronger transpiration.

Dry ecosystems usually have relatively low LAI and a higher proportion of exposed bare soil, so soil evaporation accounts for a large share of total ET. When vegetation cover or leaf area increases, the canopy plays a dual role. The simultaneous rise in Ec/ET and fall in Es/ET should

therefore be read as two outputs of the same canopy-mediated energy redistribution, not as independent trends.

Recent studies provide further support for this mechanism. Jiang et al. (2022), in their study of the Loess Plateau, found that vegetation greening intensified vegetation transpiration while constraining soil evaporation, and emphasized that the effect of greening on ET in drylands should be understood at the component level rather than only through total ET. Wang et al. (2025) similarly showed, based on a global dryland analysis, that Es accounts for an important share of dryland ET, and that vegetation change can simultaneously regulate the spatiotemporal patterns of Ec, Es, and interception evaporation (Ei). This is highly consistent with the mirror-like Ec/ET–Es/ET pattern observed in this study. Based on these mechanisms, vegetation greening in dry ecosystems should not be interpreted simply as an increase in transpiration. Rather, under limited water and energy availability, part of the energy pathway that previously supported bare-soil evaporation is redirected toward vegetation transpiration. The observed pattern therefore represents component substitution within ET, rather than a substantial expansion of total ET.

However, this energy redistribution mechanism cannot be explained by LAI change alone. The very low R^2 between the LAI trend and the Ec/ET trend (0.023) indicates that LAI is more likely to provide a directional signal for component substitution, rather than serving as the dominant controlling factor. The magnitude and spatial distribution of this substitution are more strongly determined by water availability and other non-vegetation processes.

This can be understood at several levels. First, water constraints on global vegetation growth have been increasing in recent decades (Jiao et al., 2021). The relationship between LAI and ET components is therefore not a stable linear relationship, but increasingly depends on water availability itself. Second, Fu et al. (2024) further showed that plant water stress is governed by a critical soil moisture threshold with substantial spatial heterogeneity. Below this threshold, stomatal regulation constrains transpiration, meaning that the same magnitude of LAI change may generate very different transpiration responses under different soil moisture conditions. This helps explain why the spatial variability of Ec/ET trends in dry ecosystems cannot be well captured by LAI trends alone. In addition, source-water dynamics associated with permafrost thaw and seasonal recharge represent an additional regulatory layer in high-latitude dry ecosystems. Park et al. (2021) showed that precipitation and permafrost-originated waters contribute separately and measurably to ET, suggesting that shifts in root-zone water sources can shape growing-season ET processes even where LAI change is weak. Nicholls and Carey (2021) likewise found, in a subarctic catchment, that ET differences along a forest–shrub gradient were determined not only by vegetation structure, but also by snowmelt recharge and growing-season water deficit. These findings point to seasonal hydrological processes as a necessary part of the picture, not an add-on to leaf area change. The baseline increase in Ec/ET in dry ecosystems is therefore better read as a reorganization driven by vegetation structure, water supply, and atmospheric demand acting together, rather than a straightforward greening effect.

In wet ecosystems, trends in both Ec/ET and Es/ET were close to zero, largely because wet regions tend to have more water available and both LAI and the transpiration fraction sit at higher baseline levels to begin with. Under these conditions, any transpiration gain from additional leaf area can be partly cancelled out by a rise in canopy interception loss. The near-zero trend does not mean wet pixels are insensitive to greening. The pixel-level sensitivity analysis in §5.1.2 in fact shows the opposite at the low-LAI end: when LAI is around 0.2 m^2 m^{-2}, $\partial ET/\partial LAI$ in wet ecosystems is about 1.5 times higher than in dry ecosystems. In other words, where water is not the limiting factor, the same increment in leaf area produces a noticeably larger ET response. The reason this does not translate into a detectable domain-wide trend is simply that very few wet pixels are at such low LAI; most wet pixels already sit on the saturated tail of the sensitivity curve, where additional LAI no longer matters much. The marginal effect of greening on ET thus depends on two things, not one — how dense the canopy already is, and how much water is available in the background. At the same time, because soil evaporation has already been suppressed under relatively dense canopy cover, the remaining potential for further reduction in Es is limited. Detectable shifts in component fractions therefore become less likely. Helbig et al. (2020) showed that boreal peatlands and wetland systems can maintain strong evaporative cooling even under high vapour pressure deficit, suggesting that ET in these ecosystems is closer to an energy-limited rather than water-limited state. Their ET component structure is therefore expected to be less sensitive to small LAI fluctuations. The absence of a significant component-substitution signal in wet ecosystems is therefore more likely to indicate that these systems are already in a relatively stable high-transpiration partitioning state, where marginal vegetation change is insufficient to trigger detectable internal restructuring of ET.

Whether these hydrological processes actually leave a statistical signal in ET cannot be judged from the partitioning analysis alone. The H3 partial correlation adds ESA-CCI soil moisture and ERA5-Land precipitation as additional drivers. Both have negative and statistically significant partial correlations with monthly ET anomalies, and this result is stable across FLUXCOM-X-BASE and GLEAM v4.2a. The pattern supports the interpretation that part of the LAI-independent residual reflects water-supply processes rather than vegetation change. One feature, however, runs against expectation. The soil moisture correlation is stronger in wet pixels than in dry pixels under both products. If dry ecosystems were the more water-constrained group at this timescale, the opposite ordering would be expected. This mismatch is examined further below.

6.2 Latitudinal Differentiation in the Nonlinear Temperature–ET Response

In the domain-wide analysis, both dry and wet ecosystems exhibit a cold-end breakpoint at approximately −9°C. This breakpoint indicates that when temperature anomalies fall to a sufficiently low level, the response of ET to further cooling becomes strongly weakened. This pattern more likely reflects a seasonal floor on ET in high-latitude ecosystems during cold anomalies. When temperatures are unusually low, liquid water availability for evaporation falls, vegetation physiological activity slows, and atmospheric evaporative demand weakens. ET effectively bottoms out. Once near this floor, further cooling has little room to drive additional

decline. The cold-end breakpoint is therefore better read as a low-temperature floor effect, not as evidence of warm-end water limitation.

The latitude-band analysis shows a sharper picture. At 65–75°N, ET continues to rise past the cold-end plateau in both ecosystem types, consistent with warming still operating mainly through increased available energy and atmospheric demand rather than triggering water stress. Moving into the 55–65°N band, dry ecosystems begin to flatten at the high positive-anomaly end, hinting that some pixels are nearing a water-supply ceiling. The shift is clearest in the 45–55°N band, where the breakpoint moves to the warm end and bin means turn downward once positive anomalies grow large enough, forming an inverted-U pattern.

This pattern reflects the transition from an energy-limited to a water-limited regime (Seneviratne et al., 2010). When soil moisture cannot keep up with atmospheric demand, ET stops tracking temperature. The shift is already widespread across terrestrial ecosystems, although the moisture threshold at which it occurs varies substantially across space (Denissen et al., 2022; Fu et al., 2024). At modest positive anomalies in the 45–55°N band, warming still enhances ET. Beyond a certain threshold, the widening gap between supply and demand suppresses it.

Mean growing-season LST patterns reinforce this interpretation. The 15°C and 20°C isotherms divide the domain into thermally distinct zones with different baseline risk of water stress. Most of the 65–75°N band sits under a cold growing-season background, so a positive temperature anomaly there mainly signals a relaxation of cold limitation. The 45–55°N band, by contrast, already occupies the warmer end of the domain, and the same +5°C or +8°C anomaly is more likely to push VPD and water deficit into a constraining range. The physical meaning of a given temperature anomaly is therefore not fixed. It depends on where in the temperature distribution the ecosystem already sits.

In the 45–55°N band, wet ecosystems also show a partial warm-end decline. This likely reflects how "wet" is defined here, not a shared water-limitation mechanism with dry ecosystems. GLWD records wetland area fraction. Whether a pixel is actually energy- or water-limited at the process level is a different question, and the two do not always align. A pixel flagged as wet can still face high VPD, a declining water table, or shallow soil moisture stress during anomalously warm months, especially when it sits within a broadly dry landscape.

Existing observational studies also support this interpretation. Helbig et al. (2020) found that boreal peatlands can sustain high ET under high-VPD conditions, but noted that this response depends on continuous water availability and does not hold across all warm conditions. Lafleur and Humphreys (2018) also found that higher shrub cover at tundra shrub sites did not necessarily lead to stronger latent heat flux; in some cases, the extra absorbed energy went into sensible heat instead. Mekonnen et al. (2021) reached a similar conclusion in their review of Arctic shrubification, noting that how vegetation change affects ET depends heavily on local moisture supply. Together, these findings suggest that once water supply can no longer sustain atmospheric demand, the ET response plateaus or reverses, regardless of whether vegetation cover is increasing. Permafrost hydrology may further modulate this latitudinal contrast, with

meltwater inputs potentially buffering warm-end ET suppression where permafrost remains largely intact while the fragmented permafrost across 45–55°N offers little such buffering (Park et al., 2021), although direct soil moisture and active-layer data would be required to confirm this mechanism.

The results point to a thermal threshold that moves with latitude. The cold-end breakpoint reflects a physical lower bound on ET activity at the low-temperature end, whereas the warm-end inflection first appears in the 45–55°N band, where ecosystems sit closest to the energy-to-water limitation transition. The partial warm-end signal observed in wet ecosystems further suggests that the GLWD-based dry/wet classification cannot fully represent the actual state of water limitation. Whether and where warm-end suppression appears depends on the thermal background, water supply, and latitudinal position of a given pixel, not simply on whether it carries a dry or wet label.

6.3 Driver Attribution: Latitude Outweighs the Dry–Wet Contrast

6.3.1 The H3 Predictions Did Not Hold as Stated

The four predictions in §2.2 share a common underlying assumption that dry ecosystems are more water-limited and wet ecosystems more energy-limited, and that the structure of ET drivers should therefore differ in a hierarchically recognisable way between the two classes. However, none of the four predictions held strictly across both ET products. Predictions (i) and (iii) ran opposite to what was expected: under both FLUXCOM-X-BASE and GLEAM v4.2a, the soil moisture partial correlation was stronger in wet pixels than in dry pixels, and the soil-moisture-dominant share was also larger in wet pixels. Prediction (ii) showed almost no dry–wet difference in LST partial correlation; the largest gap was 0.03, well below the wet-over-dry asymmetry the prediction called for. Prediction (iv) held for LST, but the LAI-dominant share fell by about half between the two products. The premise that the dry–wet split is the main axis of ET driver differentiation therefore does not hold under the partial correlation analysis. This does not mean the physical reasoning behind the predictions is wrong. Two separate issues are worth pulling apart, and they can both be true at once.

The first is the classification itself. The GLWD-based mask separates pixels by wetland fraction, not by how water-limited they are month by month. A pixel with a wetland fraction at or above 0.50 can still dry out locally during the middle of the growing season; a pixel below 0.50 can receive enough water from snowmelt or from a thawing active layer to mask any water-limitation signal at the monthly scale. The full argument is given in §6.4.2.

The second is the time scale of partial correlation. The framework used here compares ET anomalies with driver anomalies from one month to the next. The water-limitation mechanisms that motivated the dry–wet contrast in the first place build up over a full season or across several years. If the dry–wet difference is concentrated at those longer scales, it can be invisible in a monthly framework even when it is physically real. This is taken up in §6.4.3.

6.3.2 Latitude Outweighs the Dry–Wet Contrast

In the latitude-band analysis, within any single latitude band the largest dry–wet difference is 0.08 for SM and below 0.05 for every other driver, all smaller than the spread of the same driver across latitude. Latitude, in other words, separates ET driver structure more sharply than the dry–wet classification does.

A reasonable reading is that monthly anomaly coupling tightens at higher latitudes because the growing season is shorter there. At 65–75°N, MJJAS covers almost the entire active growing season, so monthly anomalies are anomalies within an active growing season rather than being diluted by dormant months. At 45–55°N, MJJAS is only part of a longer growing season, and monthly anomalies are spread across a wider range of background states, which weakens the monthly signal. Because LST, SM and albedo all follow the seasonal cycle closely, their partial correlations strengthen with latitude in parallel.

This pattern looks opposite to the latitudinal finding from H2, but the two are not measuring the same thing. H2 showed that in the 45–55°N dry band, high LST values stopped translating into proportionally higher ET, meaning that water limitation truncated the marginal effect of warming. H3 finds a weaker LST partial correlation in the same band. The reason is that H2 looks at the shape of the absolute response curve and asks whether ET keeps rising monotonically with LST; H3 looks at how closely monthly anomalies move together. At 65–75°N, temperature still sits in the near-linear "more warmth = more ET" regime, and monthly LST anomalies translate cleanly into ET anomalies. At 45–55°N, the effect of LST on ET is truncated at the warm end, so a positive LST anomaly does not always produce a same-sign ET anomaly, and the partial correlation weakens. Read this way, H2 and H3 sit within the same physical picture.

The albedo signal provides an additional illustration of this latitudinal gradient. The albedo partial correlation reverses sign with latitude: in the 45–55°N band, the median is +0.10 (dry) and +0.07 (wet); by 65–75°N, it flips to −0.06 (dry) and −0.13 (wet). At low latitudes, albedo anomalies mainly reflect the contrast between vegetated and bare-soil surfaces, but in the partial correlation framework LAI absorbs most of the explanatory power associated with vegetation structure, leaving a weak and slightly positive albedo residual. At high latitudes, early MJJAS months can still be affected by residual snow and early phenology: a low-albedo month means snow melted early, the growing season started sooner, and more radiation reached the surface, leading to higher ET. The two form a clear negative correlation that survives the partial correlation.

6.3.3 SM, Precip, and LAI Signals at the Monthly Scale

The SM partial correlation was stronger in wet pixels than in dry pixels under both ET products, and the SM-dominant share showed the same wet > dry pattern. In principle, if dry ecosystems were more water-limited at this time scale, SM anomalies should couple with ET anomalies more tightly in dry pixels than in wet pixels. The data show the opposite. A consistent reading is that at the monthly scale, SM tracks cloud cover and radiation more closely than it tracks water supply. A month with a positive SM anomaly is usually a month with more rain, more cloud, less sunlight reaching the surface, and lower vapour pressure deficit. ET tends to drop

in such months rather than rise, which is also why the SM partial correlation is negative throughout this study. The drop is sharper in wet pixels because their ET is mainly limited by how much energy is available, so when a wet month brings clouds and low radiation, the main driver of their ET weakens and ET falls steeply. Dry pixels behave differently in the same month: their ET is more often held back by background water storage and vegetation state, so a short-term dip in radiation has less effect on them.

The same logic extends to Precip, whose median partial correlation ranges from −0.10 to −0.21 across products and ecosystem classes. Months with positive Precip anomalies are months with more cloud and lower radiation, so Precip–ET also comes out negative through the same indirect coupling. The monthly anomaly framework has a built-in limitation here. The physical picture behind predictions (i) and (iii) is that dry ecosystems are more water-limited, and this limitation operates at seasonal-to-interannual accumulation scales: multi-year deficits in root-zone water storage, cumulative precipitation shortfall over the growing season, and potential water sources from active-layer thaw. These processes do not appear directly in single-month SM or Precip anomalies; they only emerge under longer-term integration. A monthly SM–ET coupling can also reflect either soil moisture limiting ET or ET drying down soil moisture (Berg & Sheffield, 2019), and the signal itself does not therefore correspond directly to the seasonal water-storage limitation that dry-ecosystem theory has in mind (Orth & Seneviratne, 2013; Seneviratne et al., 2010). The negative sign and the absent dry–wet contrast do not falsify the physical picture; they only show that the monthly anomaly framework is not the right tool for testing it.

The LAI signal carries a different methodological caveat. Under FLUXCOM-X-BASE, LAI is the dominant driver in 75% of dry pixels and 65% of wet pixels; under GLEAM v4.2a, these shares fall to 34% and 29%, with the median LAI partial correlation dropping from +0.50 / +0.47 to +0.27 / +0.24. LAI remains the largest positive term among the five drivers under both products, but the share itself is cut roughly in half. This product dependence comes largely from the training structure of FLUXCOM-X-BASE: X-BASE upscales FLUXNET eddy-covariance observations to global grids via XGBoost, with training features that include MODIS LST and MODIS-reflectance-derived vegetation indices (Nelson et al., 2024), and the LAI product used here (MOD15A2H) shares the underlying MODIS reflectance signal with these training features. This overlap means that the FLUXCOM-X-BASE ET estimates naturally echo the LAI signal in the data; once ET is replaced by GLEAM v4.2a, this echo is stripped away, and the share that LAI gives up is taken over mostly by SM, LST, and Albedo, while Precip barely changes.

6.4 Methodological Considerations

6.4.1 FLUXCOM-X-BASE Predictor Circularity

The primary methodological concern is predictor circularity in the partial correlation analysis. FLUXCOM-X-BASE is constructed by upscaling FLUXNET eddy-covariance observations to global grids via XGBoost, with a predictor set that includes MODIS LST and MODIS-based

vegetation indices (Nelson et al., 2024). The overlap between this predictor set and the five H3 drivers is uneven. MODIS LST enters the analysis twice: once as an H3 driver and once as a training predictor for the ET product against which it is correlated. The overlap with LAI is weaker but present, since MODIS vegetation indices and MOD15A2H LAI share underlying spectral information. MCD43A3 albedo is not part of the predictor set. ERA5-Land precipitation is not a direct predictor either, but it shares the ERA5 reanalysis backbone with FLUXCOM-X-BASE's meteorological forcing, so a partial overlap at the forcing level remains. ERA5-Land soil water (swvl1) is the only one of the five drivers fully independent of the predictor set.

Predictor circularity affects the three hypotheses differently, and the difference matters for how much weight to place on each set of results. For H1, the core finding concerns long-term redistribution among ET components estimated from GLEAM, not from FLUXCOM-X-BASE; total ET from FLUXCOM-X-BASE enters only as a comparator, so circularity does not compromise the component-substitution result. H2 is more exposed: MODIS LST in the training set may inflate the apparent temperature sensitivity of FLUXCOM-X-BASE ET, but the analysis targets the shape and latitudinal variation of the binned response curve rather than ranking independent drivers, which limits the distortion. The partial correlation analysis for H3 is where the circularity bites hardest, because three of the five candidate drivers (LST, LAI, and Precip) overlap with the predictor set to varying degrees. The FLUXCOM-based partial correlations for H3 should therefore be read as product-conditioned statistical associations, not as independent causal attribution.

ERA5-Land SM is the exception. Because it does not enter the FLUXCOM-X-BASE predictor set, its negative partial correlation under that product is not inflated by training overlap. The same direction reappears under GLEAM v4.2a, where ERA5-Land SM is also not a primary input. The negative coupling between SM and ET discussed in §6.3.3 is therefore a cross-product feature of the data, not a shared artifact of training structure.

The GLEAM v4.2a sensitivity check was designed to test how much of the H3 result survives when the ET product is changed. Unlike FLUXCOM-X-BASE, GLEAM derives land evaporation through a process-based framework rather than by training directly on MODIS LST and vegetation indices (Miralles et al., 2025b). Its output covers transpiration, bare-soil evaporation, interception loss, and evaporative stress as separate components. Switching to GLEAM shifted the dominant-driver distribution substantially: the no-significant-driver class expanded, LAI-dominant pixels contracted, and LST-dominant pixels increased. At the level of median partial correlations, the picture was less categorical. LAI remained positively associated with ET anomalies but with markedly weaker coefficients than under FLUXCOM-X-BASE; the LST partial correlation was more stable across the two products.

Taken together, these results indicate that the categorical LAI-dominance map is partly a function of FLUXCOM-X-BASE's predictor structure, while the association of both LAI and LST with ET anomaly variability is real enough to survive a product change, even if the magnitudes shift. GLEAM is not a clean independent benchmark for this purpose...A fully independent validation of H3 would require an ET estimate derived from a substantially

different observational constraint, such as a water-balance approach using GRACE-based terrestrial water storage change. Such an analysis is beyond the scope of this thesis, but it would be an important direction for future work.

6.4.2 The Scope and Limits of the GLWD Classification

A second methodological limitation concerns the interpretation of the GLWD-based dry–wet classification. Wet pixels were defined here as those with a GLWD wetland fraction at or above 50%. This threshold captures hydromorphological wetness, wetland extent, surface saturation, and the contrast between peatland landscapes and upland areas. It is ecologically meaningful in boreal and Arctic settings. It does not, however, indicate whether a pixel is energy-limited or water-limited at the process level, which is the distinction H2 and H3 are built around.

The H3 results provide direct evidence of this mismatch. Under both FLUXCOM-X-BASE and GLEAM v4.2a, the SM–ET partial correlation is stronger in wet pixels than in dry pixels. If the GLWD-defined dry class corresponded to water-limited ecosystems, dry pixels should show the tighter SM–ET coupling instead. The empirical signal points the other way, which confirms that GLWD wetness does not function as a proxy for water limitation.

The underlying reason is that hydromorphological wetness and process-based water limitation describe different things. A GLWD-dry pixel may sit in a precipitation-rich boreal forest where growing-season ET is held back by available energy, not water supply. A GLWD-wet pixel may run into temporary water stress during high-VPD periods, when the local water table drops or shallow soil moisture runs low. Process-level water limitation emerges from the joint state of soil moisture, atmospheric demand, vegetation hydraulic regulation, and soil texture (Denissen et al., 2022; Fu et al., 2024; Wankmüller et al., 2024). Wetland fraction alone does not capture any of these.

The same mismatch affects the interpretation of H1 and H2. The similar LAI–Ec/ET slopes across dry and wet ecosystems in H1 partly reflect that the GLWD dry class includes precipitation-rich forested uplands. The warm-end inflection in 45–55°N wet pixels likewise points to wet pixels sharing the thermal background of neighbouring dry ones rather than to a shared water-limitation mechanism.

Latitude and absolute thermal regime appear to capture the energy-to-water limitation transition more directly than the binary GLWD classification. The warm-end ET inflection emerges first at 45–55°N, and the LST partial correlation strengthens with latitude. A more process-aligned stratification, based on aridity index, Budyko-type dryness ratios, or thresholds in soil moisture and VPD, would better match the framing of H2 and H3. Testing the same questions under that stratification is a worthwhile next step.

6.4.3 Anomaly Framework Limits Both Threshold Detection and Storage Diagnostics

This study adopted the anomaly framework to remove spatial gradient confounding from the temperature–ET response analysis. If absolute LST and ET values had been pooled across the

full study domain, the resulting curve would have been dominated by geography rather than by within-pixel temperature sensitivity. Subtracting each pixel's monthly climatology shifts the analysis onto local departures from the seasonal baseline.

The cost is that the anomaly transformation strips out absolute temperature information, which is what matters for detecting warm-end water limitation. A +5°C anomaly at 45–55°N may signal genuinely hot conditions, while the same +5°C anomaly at 65–75°N may signal only a break from cold limitation. The framework places both observations in the same bin. The domain-wide analysis therefore recovered a cold-end breakpoint rather than the warm-end threshold H2 predicted. Latitude banding narrows the spread of absolute conditions within each bin, but it does not recover the information the anomaly transformation removed.

A cleaner H2 design would bin by absolute LST within each latitude band rather than by anomaly. VPD could be added as a second explanatory variable, since it tracks atmospheric demand more directly than LST does. Soil moisture should also enter the framework, because water limitation depends on the joint state of soil moisture, atmospheric demand, and soil hydraulic properties (Fu et al., 2024; Wankmüller et al., 2024). The anomaly framework similarly limits H3, since monthly partial correlations cannot capture the seasonal to interannual accumulation of water limitation invoked by predictions (i) and (iii); storage-based metrics such as cumulative precipitation deficits or GRACE-derived root-zone water storage anomalies would be more appropriate for that test.

6.4.4 Missing Soil Moisture and Partial-Correlation Limits

Even with five drivers included, the H3 partial-correlation framework still faces two structural limits. Partial correlation isolates how ET co-varies with one target variable within the linear space spanned by the included predictors. Variables left outside this space stay neither controlled nor identified. Take VPD. LST may act on ET partly through VPD and partly through other pathways, and a model without VPD cannot tell them apart (Byrnes & Dee, 2025).

The second limit concerns how dominant drivers were identified. A driver was classified as dominant for a given pixel when its partial correlation passed $p < 0.05$. The t-test underlying this threshold becomes easier to pass as the sample size grows, and with 100 monthly observations per pixel a partial correlation as small as $|r| \approx 0.2$ already meets it. The dominant-driver maps in §5.3.3 therefore include pixels where the leading driver explains only a small share of ET variance. Requiring a minimum effect size, for example $|r_{partial}| > 0.3$, alongside the p-value threshold would tighten the classification to drivers with substantive rather than merely detectable associations.

7 Conclusion

Warming-induced changes in northern high-latitude ET require more than just tracking total-flux growth. To address this, I analyzed the growing-season ET characteristics across regions north of 45°N from 2001 to 2020 using multi-source remote sensing data. I focused on three interrelated questions: the potential redistribution of ET components in dry versus wet ecosystems, the existence of nonlinear temperature-ET thresholds, and the dominant drivers controlling ET anomalies across different ecosystem types.

Previous studies have largely focused on total ET and mid-to-low latitude thresholds, often relying on single remote sensing products. This leaves gaps regarding component redistribution, warm-end water limitation in high latitudes, and the biases introduced by training structures in ET datasets. My analysis reveals a distinct component-substitution pattern in dry ecosystems. The transpiration fraction increases while the soil evaporation fraction decreases, with median trends nearly symmetric in magnitude (+0.000132 and -0.000130 yr^{-1}, respectively). Wet ecosystems do not show this systematic change. Interestingly, regressing these component trends against LAI trends yields an R^2 of only 0.023. This indicates that while the reorganization aligns directionally with vegetation greening, non-vegetation processes primarily govern it quantitatively. The consistency of the total-ET trend across FLUXCOM-X-BASE and GLEAM v4.2a confirms this is a physical redistribution rather than a statistical artifact.

Regarding temperature thresholds, domain-wide data challenges the expectation of a strict warm-end water limitation. I instead observed a cold-end breakpoint near -9°C. This breakpoint reflects the physical lower bound imposed by snow cover and vegetation dormancy. The anticipated warm-end threshold only appears when stratifying by latitude. In the 45–55°N band, dry ecosystems show a clear decline in ET at the warm extreme. This suggests that water-limitation thresholds follow a latitudinal gradient, which is currently active at lower latitudes but likely to move poleward with Arctic amplification.

Furthermore, data overturns the initial hypothesis that dry and wet ecosystems have strictly partitioned driver structures. The latitudinal gradient differentiates ET drivers much more sharply. LST correlations systematically strengthen toward higher latitudes across different products. While soil moisture consistently shows a negative partial correlation, it manifests more strongly in wet ecosystems than in dry ones at the monthly scale, defying classical water-limitation assumptions.

Finally, I found that the strong dominance of LAI and LST signals under FLUXCOM-X-BASE partly results from predictor circularity. Its machine-learning framework is intrinsically trained on MODIS-derived features. This structural overlap explains the divergent driver attribution when compared to the physics-based GLEAM model. By synthesizing the cross-product consistency in total-flux trends with the product-sensitivity in driver attribution, this study highlights a methodological takeaway. Single-product causal inference in large-scale ET research is unreliable. Future studies must evaluate the internal structural assumptions of remote sensing products alongside statistical validation.

References

Berg, A., & Sheffield, J. (2019). Historic and Projected Changes in Coupling Between Soil Moisture and Evapotranspiration (ET) in CMIP5 Models Confounded by the Role of Different ET Components. *Journal of Geophysical Research: Atmospheres*, *124*(11), 5791–5806. https://doi.org/10.1029/2018JD029807

Berner, L. T., Massey, R., Jantz, P., Forbes, B. C., Macias-Fauria, M., Myers-Smith, I., Kumpula, T., Gauthier, G., Andreu-Hayles, L., Gaglioti, B. V., Burns, P., Zetterberg, P., D'Arrigo, R., & Goetz, S. J. (2020). Summer warming explains widespread but not uniform greening in the Arctic tundra biome. *Nature Communications*, *11*(1), 4621. https://doi.org/10.1038/s41467-020-18479-5

Bhatt, U. S., Walker, D. A., Raynolds, M. K., Bieniek, P. A., Epstein, H. E., Comiso, J. C., Pinzon, J. E., Tucker, C. J., Steele, M., Ermold, W., & Zhang, J. (2017). Changing seasonality of panarctic tundra vegetation in relationship to climatic variables. *Environmental Research Letters*, *12*(5), 055003. https://doi.org/10.1088/1748-9326/aa6b0b

Bonan, G. B. (2008). Forests and Climate Change: Forcings, Feedbacks, and the Climate Benefits of Forests. *Science*, *320*(5882), 1444–1449. https://doi.org/10.1126/science.1155121

Bonfils, C. J. W., Phillips, T. J., Lawrence, D. M., Cameron-Smith, P., Riley, W. J., & Subin, Z. M. (2012). On the influence of shrub height and expansion on northern high latitude climate. *Environmental Research Letters*, *7*(1), 015503. https://doi.org/10.1088/1748-9326/7/1/015503

Budyko, M. I. (1974). *Climate and Life*. Academic Press.

Burnham, K. P., Anderson, D. R. (2002). *Model selection and multimodel inference: A practical information-theoretic approach* (2nd ed). Springer.

Byrnes, J. E. K., & Dee, L. E. (2025). Causal Inference With Observational Data and Unobserved Confounding Variables. *Ecology Letters*, *28*(1), e70023. https://doi.org/10.1111/ele.70023

Chapin, F. S., Sturm, M., Serreze, M. C., McFadden, J. P., Key, J. R., Lloyd, A. H., McGuire, A. D., Rupp, T. S., Lynch, A. H., Schimel, J. P., Beringer, J., Chapman, W. L., Epstein, H. E., Euskirchen, E. S., Hinzman, L. D., Jia, G., Ping, C.-L., Tape, K. D., Thompson, C. D. C., … Welker, J. M. (2005). Role of Land-Surface Changes in Arctic Summer Warming. *Science*, *310*(5748), 657–660. https://doi.org/10.1126/science.1117368

Copernicus Climate Change Service. (2019). *ERA5-Land monthly averaged data from 1950 to present* [Dataset]. Copernicus Climate Change Service (C3S) Climate Data Store (CDS). https://doi.org/10.24381/CDS.68D2BB30

Denissen, J. M. C., Teuling, A. J., Pitman, A. J., Koirala, S., Migliavacca, M., Li, W., Reichstein, M., Winkler, A. J., Zhan, C., & Orth, R. (2022). Widespread shift from ecosystem energy to water limitation with climate change. *Nature Climate Change*, *12*(7), 677–684. https://doi.org/10.1038/s41558-022-01403-8

Frost, G. V., Bhatt, U. S., Macander, M. J., Berner, L. T., Walker, D. A., Raynolds, M. K., Magnússon, R. Í., Bartsch, A., Bjerke, J. W., Epstein, H. E., Forbes, B. C., Goetz, S. J., Hoy, E. E., Karlsen, S. R., Kumpula, T., Lantz, T. C., Lara, M. J., López-Blanco, E., Montesano, P. M., … Waigl, C. F. (2025). The changing face of the Arctic: Four decades of greening and implications for tundra ecosystems. *Frontiers in Environmental Science*, *13*, 1525574. https://doi.org/10.3389/fenvs.2025.1525574

Fu, Z., Ciais, P., Wigneron, J.-P., Gentine, P., Feldman, A. F., Makowski, D., Viovy, N., Kemanian, A. R., Goll, D. S., Stoy, P. C., Prentice, I. C., Yakir, D., Liu, L., Ma, H., Li, X., Huang, Y., Yu, K., Zhu, P., Li, X., … Smith, W. K. (2024). Global critical soil moisture thresholds of plant water stress. *Nature Communications*, *15*(1), 4826. https://doi.org/10.1038/s41467-024-49244-7

Good, S. P., Noone, D., & Bowen, G. (2015). Hydrologic connectivity constrains partitioning of global terrestrial water fluxes. *Science*, *349*(6244), 175–177. https://doi.org/10.1126/science.aaa5931

Helbig, M., Waddington, J. M., Alekseychik, P., Amiro, B., Aurela, M., Barr, A. G., Black, T. A., Carey, S. K., Chen, J., Chi, J., Desai, A. R., Dunn, A., Euskirchen, E. S., Flanagan, L. B., Friborg, T., Garneau, M., Grelle, A., Harder, S., Heliasz, M., … Schulze, C. (2020). The biophysical climate mitigation potential of boreal peatlands during the growing season. *Environmental Research Letters*, *15*(10), 104004. https://doi.org/10.1088/1748-9326/abab34

Helbig, M., Waddington, J. M., Alekseychik, P., Amiro, B. D., Aurela, M., Barr, A. G., Black, T. A., Blanken, P. D., Carey, S. K., Chen, J., Chi, J., Desai, A. R., Dunn, A., Euskirchen, E. S., Flanagan, L. B., Forbrich, I., Friborg, T., Grelle, A., Harder, S., … Zyrianov, V. (2020). Increasing contribution of peatlands to boreal evapotranspiration in a warming climate. *Nature Climate Change*, *10*(6), 555–560. https://doi.org/10.1038/s41558-020-0763-7

Jiang, F., Xie, X., Wang, Y., Liang, S., Zhu, B., Meng, S., Zhang, X., Chen, Y., & Liu, Y. (2022). Vegetation greening intensified transpiration but constrained soil evaporation on the Loess Plateau. *Journal of Hydrology*, *614*, 128514. https://doi.org/10.1016/j.jhydrol.2022.128514

Jiao, W., Wang, L., Smith, W. K., Chang, Q., Wang, H., & D'Odorico, P. (2021). Observed increasing water constraint on vegetation growth over the last three decades. *Nature Communications*, *12*(1), 3777. https://doi.org/10.1038/s41467-021-24016-9

Jung, M., Reichstein, M., Ciais, P., Seneviratne, S. I., Sheffield, J., Goulden, M. L., Bonan, G., Cescatti, A., Chen, J., De Jeu, R., Dolman, A. J., Eugster, W., Gerten, D., Gianelle, D., Gobron, N., Heinke, J., Kimball, J., Law, B. E., Montagnani, L., … Zhang, K. (2010). Recent decline in the global land evapotranspiration trend due to limited moisture supply. *Nature*, *467*(7318), 951–954. https://doi.org/10.1038/nature09396

Jung, M., Reichstein, M., Schwalm, C. R., Huntingford, C., Sitch, S., Ahlström, A., Arneth, A., Camps-Valls, G., Ciais, P., Friedlingstein, P., Gans, F., Ichii, K., Jain, A. K., Kato, E., Papale, D., Poulter, B., Raduly, B., Rödenbeck, C., Tramontana, G., … Zeng, N. (2017). Compensatory water effects link yearly global land CO2 sink changes to temperature. *Nature*, *541*(7638), 516–520. https://doi.org/10.1038/nature20780

Keenan, T. F., & Riley, W. J. (2018). Greening of the land surface in the world's cold regions consistent with recent warming. *Nature Climate Change*, *8*(9), 825–828. https://doi.org/10.1038/s41558-018-0258-y

Kendall, M. G. (1975). *Rank correlation methods* (4. ed., 2. impr). Griffin.

Lafleur, P. M., & Humphreys, E. R. (2018). Tundra shrub effects on growing season energy and carbon dioxide exchange. *Environmental Research Letters*, *13*(5), 055001. https://doi.org/10.1088/1748-9326/aab863

Lehner, B., Anand, M., & Fluet-Chouinard, E. (2025). *Global Lakes and Wetlands Database (GLWD) version 2.0* [Dataset]. figshare. https://doi.org/10.6084/m9.figshare.28519994.v1

Li, H., Wang, W., Chen, Z., Li, X., Mura, M., Teuling, A. J., Cescatti, A., & Forzieri, G. (2026). Weakening vegetation control on global terrestrial evapotranspiration in a warmer world. *Communications Earth & Environment*, *7*(1), 365. https://doi.org/10.1038/s43247-026-03372-8

Mann, H. B. (1945). Nonparametric Tests Against Trend. *Econometrica*, *13*(3), 245. https://doi.org/10.2307/1907187

Martens, B., Miralles, D. G., Lievens, H., van der Schalie, R., de Jeu, R. A. M., Fernández-Prieto, D., Beck, H. E., Dorigo, W. A., & Verhoest, N. E. C. (2017). GLEAM v3: Satellite-based land evaporation and root-zone soil moisture. *Geoscientific Model Development*, 10, 1903–1925. https://doi.org/10.5194/gmd-10-1903-2017

Mekonnen, Z. A., Riley, W. J., Berner, L. T., Bouskill, N. J., Torn, M. S., Iwahana, G., Breen, A. L., Myers-Smith, I. H., Criado, M. G., Liu, Y., Euskirchen, E. S., Goetz, S. J., Mack, M. C., & Grant, R. F. (2021). Arctic tundra shrubification: A review of mechanisms and impacts on ecosystem carbon balance. *Environmental Research Letters*, *16*(5), 053001. https://doi.org/10.1088/1748-9326/abf28b

Miralles, D. G., Bonte, O., Koppa, A., Baez-Villanueva, O. M., Tronquo, E., Zhong, F., Beck, H. E., Hulsman, P., Dorigo, W., Verhoest, N. E. C., & Haghdoost, S. (2025a). *GLEAM4* (Version v4.2) [Dataset]. Zenodo. https://doi.org/10.5281/zenodo.14724263

Miralles, D. G., Bonte, O., Koppa, A., Baez-Villanueva, O. M., Tronquo, E., Zhong, F., Beck, H. E., Hulsman, P., Dorigo, W., Verhoest, N. E. C., & Haghdoost, S. (2025b). GLEAM4: Global land evaporation and soil moisture dataset at 0.1° resolution from 1980 to near present. *Scientific Data*, *12*(1), 416. https://doi.org/10.1038/s41597-025-04610-y

Monteith, J. L. (1965). Evaporation and environment. *Symposia of the Society for Experimental Biology*, *19*, 205–224.

Muñoz-Sabater, J., Dutra, E., Agustí-Panareda, A., Albergel, C., Arduini, G., Balsamo, G., Boussetta, S., Choulga, M., Harrigan, S., Hersbach, H., Martens, B., Miralles, D. G., Piles, M., Rodríguez-Fernández, N. J., Zsoter, E., Buontempo, C., & Thépaut, J.-N. (2021). ERA5-Land: A state-of-the-art global reanalysis dataset for land applications. *Earth System Science Data*, *13*(9), 4349–4383. https://doi.org/10.5194/essd-13-4349-2021

Myneni, R., Knyazikhin, Y., & Park, T. (2021). *MODIS/Terra Leaf Area Index/FPAR 8-Day L4 Global 500m SIN Grid V061* [Dataset]. NASA EOSDIS Land Processes DAAC. https://doi.org/10.5067/MODIS/MOD15A2H.061

Nelson, J. A., Walther, S., Gans, F., Kraft, B., Weber, U., Novick, K., Buchmann, N., Migliavacca, M., Wohlfahrt, G., Šigut, L., Ibrom, A., Papale, D., Göckede, M., Duveiller, G., Knohl, A., Hörtnagl, L., Scott, R. L., Dušek, J., Zhang, W., … Jung, M. (2024). X-BASE: The first terrestrial carbon and water flux products from an extended data-driven scaling framework, FLUXCOM-X. *Biogeosciences*, *21*(22), 5079–5115. https://doi.org/10.5194/bg-21-5079-2024

Nicholls, E. M., & Carey, S. K. (2021). Evapotranspiration and energy partitioning across a forest-shrub vegetation gradient in a subarctic, alpine catchment. *Journal of Hydrology*, *602*, 126790. https://doi.org/10.1016/j.jhydrol.2021.126790

Olefeldt, D., Hovemyr, M., Kuhn, M. A., Bastviken, D., Bohn, T. J., Connolly, J., Crill, P., Euskirchen, E. S., Finkelstein, S. A., Genet, H., Grosse, G., Harris, L. I., Heffernan, L., Helbig, M., Hugelius, G., Hutchins, R., Juutinen, S., Lara, M. J., Malhotra, A., … Watts, J. D. (2021). The Boreal–Arctic Wetland and Lake Dataset (BAWLD). *Earth System Science Data*, *13*(11), 5127–5149. https://doi.org/10.5194/essd-13-5127-2021

Orth, R., & Seneviratne, S. I. (2013). Propagation of soil moisture memory to streamflow and evapotranspiration in Europe. *Hydrology and Earth System Sciences*, *17*(10), 3895–3911. https://doi.org/10.5194/hess-17-3895-2013

Park, H., Tanoue, M., Sugimoto, A., Ichiyanagi, K., Iwahana, G., & Hiyama, T. (2021). Quantitative Separation of Precipitation and Permafrost Waters Used for Evapotranspiration in a Boreal Forest: A Numerical Study Using Tracer Model. *Journal of Geophysical Research: Biogeosciences*, *126*(12), e2021JG006645. https://doi.org/10.1029/2021JG006645

Rantanen, M., Karpechko, A. Yu., Lipponen, A., Nordling, K., Hyvärinen, O., Ruosteenoja, K., Vihma, T., & Laaksonen, A. (2022). The Arctic has warmed nearly four times faster than the globe since 1979. *Communications Earth & Environment*, *3*(1), 168. https://doi.org/10.1038/s43247-022-00498-3

Schaaf, C., & Wang, Z. (2021). *MODIS/Terra+Aqua BRDF/Albedo Daily L3 Global—500m V061* [Dataset]. NASA Land Processes Distributed Active Archive Center. https://doi.org/10.5067/MODIS/MCD43A3.061

Sen, P. K. (1968). Estimates of the Regression Coefficient Based on Kendall's Tau. *Journal of the American Statistical Association*, *63*(324), 1379–1389. https://doi.org/10.1080/01621459.1968.10480934

Seneviratne, S. I., Corti, T., Davin, E. L., Hirschi, M., Jaeger, E. B., Lehner, I., Orlowsky, B., & Teuling, A. J. (2010). Investigating soil moisture–climate interactions in a changing climate: A review. *Earth-Science Reviews*, *99*(3–4), 125–161. https://doi.org/10.1016/j.earscirev.2010.02.004

Wan, Z., Hook, S., & Hulley, G. (2021). *MODIS/Terra Land Surface Temperature/Emissivity 8-Day L3 Global 1km SIN Grid V061* [Dataset]. NASA EOSDIS Land Processes DAAC. https://doi.org/10.5067/MODIS/MOD11A2.061

Wang, L., Good, S. P., & Caylor, K. K. (2014). Global synthesis of vegetation control on evapotranspiration partitioning. *Geophysical Research Letters*, *41*(19), 6753–6757. https://doi.org/10.1002/2014GL061439

Wang, S., Zhu, C., Huang, Z., Li, Y., Cui, C., & Zhang, C. (2025). Primary roles of soil evaporation and vegetation in driving terrestrial evapotranspiration across global drylands. *Science of The Total Environment*, *958*, 178073. https://doi.org/10.1016/j.scitotenv.2024.178073

Wankmüller, F. J. P., Delval, L., Lehmann, P., Baur, M. J., Cecere, A., Wolf, S., Or, D., Javaux, M., & Carminati, A. (2024). Global influence of soil texture on ecosystem water limitation. *Nature*, *635*(8039), 631–638. https://doi.org/10.1038/s41586-024-08089-2

Yang, Y., Roderick, M. L., Guo, H., Miralles, D. G., Zhang, L., Fatichi, S., Luo, X., Zhang, Y., McVicar, T. R., Tu, Z., Keenan, T. F., Fisher, J. B., Gan, R., Zhang, X., Piao, S., Zhang, B., & Yang, D. (2023). Evapotranspiration on a greening Earth. *Nature Reviews Earth & Environment*, *4*(9), 626–641. https://doi.org/10.1038/s43017-023-00464-3

Zhang, W., Jansson, C., Miller, P. A., Smith, B., & Samuelsson, P. (2014). Biogeophysical feedbacks enhance the Arctic terrestrial carbon sink in regional Earth system dynamics. *Biogeosciences*, *11*(19), 5503–5519. https://doi.org/10.5194/bg-11-5503-2014